# NUCLEAR BETA SPECTROSCOPY USING SOLID STATE DETECTORS

Thesis by

John Michael Trischuk

In Partial Fulfillment of the Requirements

For the Degree of

Doctor of Philosophy

California Institute of Technology
Pasadena, California

1967

(Submitted June 24, 1966)

## ACKNOWLEDGMENTS

The author would like to thank Dr. E. Kankeleit for his consistent encouragement and criticism during all phases of this work, Dr. F. Boehm for his suggestion of the problem and support during the early stages of the work, and Mrs. K. Ryde for her assistance with the chemical separation. He would also like to thank E. Seltzer and R. Hager for reading the manuscript and aid in the computation of electron wavefunctions, D. Bowman for numerous discussions concerning the data analysis, and Barbara Curtis for her kind understanding.

# ABSTRACT

The beta decay shape factor of the 4.8 minute isotope $Tl^{207}$ is measured to be $(.0423 \pm .0006)(1 + (.024 \pm .010)W)$ using solid state detectors. The result is interpreted in terms of the shell model. The properties of the solid state beta spectrometer are described.

# TABLE OF CONTENTS

# I. INTRODUCTION

The study of the emission of beta particles from nuclei is one of the oldest in nuclear physics. The beta particles are unique amongst the nuclear radiations in that they are emitted in a continuous spectrum. By the 1930's the work with magnetic spectrometers had provided much information concerning the distribution in momentum of the emitted beta particles. By this time the peaks observed in the beta spectra of some nuclei had been correctly identified as atomic electrons associated with the internal conversion of the gamma rays emitted by these nuclei. In 1927 Pauli suggested the existence of the neutrino to explain the continuous distribution of beta particles without abandoning the principle of conservation of energy.

The first theoretical explanation of beta decay was put forward in 1934 by Fermi$^{1)}$, and his basic hypothesis is believed to be correct. He proposed that the process be described by the interaction of the nuclear current with the lepton current, in analogy to the electromagnetic interaction where the nuclear current interacts with the electromagnetic field. In the case of beta decay the two leptons can be emitted in a singlet or triplet state, which leads to two types of transitions, Fermi and Gamow-Teller, each with its own coupling constant.

The currents involved in the beta decay process can be formed in five different ways. In Fermi's original formulation he constructed the currents as four vectors. This was generalized to include scalar, tensor, pseudo-vector and pseudo-scalar currents, with arbitrary strengths. The interaction Hamiltonian was then written in the form $\sum_{\beta} C_{\beta}\langle\bar{\psi}_p O_{\beta}\psi_n\rangle\langle\bar{\psi}_e O_{\beta}\psi_{\nu}\rangle$ . The last major change in this interaction Hamiltonian came when Lee and Yang[2)] advanced the hypothesis that parity was not conserved in the weak interactions. This necessitates the addition of the terms $C'_{\beta}\langle\bar{\psi}_p O_{\beta}\psi_n\rangle\ \langle\bar{\psi}_e O_{\beta}\gamma_5\psi_{\nu}\rangle$.

In this state the beta interaction contains ten possible coupling constants. The subsequent experimental effort was devoted primarily to measuring these coupling strengths. The ratio of the Fermi to Gamow-Teller coupling constants is relatively simple to determine. One looks at the "comparative half-life" $(ft)_{1/2}$ of transitions in which the initial and final spins are zero, such as $O^{14}$, $Al^{26}$ and $Cl^{34}$, in which only the Fermi interaction is allowed and compares this to the $(ft)_{1/2}$ value for the decay of the neutron, where both interactions occur. From this one obtains $|C_{GT}|^2/|C_F|^2 = 1.46 \pm .06$.

Determination of the relative sizes of the ten coupling constants $C_{\beta}$ and $C'_{\beta}$ requires much more sophisticated experiments. By measuring the polarization of the beta rays emitted from $Co^{60}$ to be $-\frac{v}{c}$, Frauenfelder[3)] showed that the spin of the electron is antiparallel to its motion, in the limit of high velocity. This allows the conclusion $C_{\beta} = C'_{\beta}$ which is described as maximum parity violation. Electron-neutrino angular correlation studies[4,5)] showed that the neutrino is also emitted with its spin antiparallel to its motion, which leads to the conclusion that only the vector and axial-vector parts of the interaction contribute to the beta decay process. The final important experiments in this connection were the measurement of the polarization of the protons following the beta decay of the neutron$^{6)}$. These experiments show that $C_V = - 1.2\ C_A$.

The basic results of this activity are that the Fermi and Gamow-Teller coupling constants are approximately equal, that the parity non-conserving coupling constant $C'_\beta$ equals the parity conserving coupling constant $C_\beta$, and that only the vector and axial-vector interactions contribute in the combination V-A. The slight deviation from this statement of the form of the beta interaction (actually $|C_{GT}|^2/|C_F|^2 = 1.46$ and $C_V = - 2\ C_A$) is a subject of the most recent investigations in beta decay$^{6a,6b)}$.

From the point of view of the nuclear physicist the beta interaction can be considered known. The measurement of $(ft)_{1/2}$ values, shape factors, electron-neutrino correlations and polarizations then determine various combinations of nuclear matrix elements. In transitions where the initial and final spins are zero only one matrix element enters in the allowed case, and two in the first forbidden case, hence one can usually determine these matrix elements. In most cases, there are two matrix elements that contribute to allowed decays, and as many as six matrix elements in first forbidden decays. Here the problem of determining those parameters by experiment is in general very difficult. In regions of the periodic table where good descriptions of a nucleus exist one can reduce the number of free parameters by using a nuclear model. In this way the experiments can be used to check the assumptions of the model.

The techniques for obtaining information about the shape of beta spectra have centered around the magnetic spectrometer. These spectrometers first appeared around 1920, and had as their main attribute high momentum resolution, commonly less than .1%. This resolution is obtained at the expense of reducing the effective solid angle subtended by the detector to about 1 percent of the whole sphere, which has been a serious limiting factor to the experiments which can be done with this instrument. The development of solid state detectors offers the possibility of constructing a spectrometer which complements the properties of the magnetic spectrometer. Such a spectrometer offers the advantage of $4\pi$ counting geometry, energy resolution in some cases comparable to magnetic spectrometers, and low time resolution for coincidence experiments.

In the last ten years much work has been done on the development of solid state detectors and their associated electronics for the purpose of studying nuclear radiations. The work has been primarily concerned with increasing the energy resolution obtainable with the view to studying alpha, gamma, and conversion electron spectra, and the products of nuclear reactions. At the present very little data is available on their use in the study of continuous beta spectra.

The work to be described in this thesis was undertaken to examine the effects which can lead to distortions in measured beta spectra. The object was to construct a spectrometer which could be used with confidence in determining the shape factors of short lived isotopes, specifically the 4.8 minute $Tl^{207}$. On the basis of single particle model estimates, the deviation from an allowed shape, i.e., the shape factor, was expected to be about 5 percent per MeV.

Investigations using a single detector show that due to environmental effects the fraction of electrons backscattered from the environment can become as high as 2 1/2 times the fraction backscattered from silicon alone. We describe shape factor measurements with $Pr^{143}$ and $Bi^{210}$ using this geometry. Although the results obtained are in agreement with previous work, the accuracy with which shape factors can be determined is not good. Using $4\pi$ geometry we investigated effects of source absorption and detector separation. Both of these effects can introduce corrections to the shape factor which are as big as the shape factor of $Tl^{207}$. As a test case we have measured the shape factor of $P^{32}$ and obtain excellent agreement with measurements using magnetic spectrometers.

Using this spectrometer we have measured the shape factor of $Tl^{207}$. The results are compared to shell model predictions. Although one has a good model with which to compute matrix elements the shell model calculation leads to too low an $(ft)_{1/2}$ value and too large a shape factor. We discuss these discrepancies in terms of configuration mixing resulting from a polarization of the core by the single particle. The effect of this configuration mixing is to reduce the size of the vector matrix elements. The result can be understood by assuming the "effective beta charges" are less than the single particle contribution.

## II. SOLID STATE DETECTORS

### i) Historical Note

The discovery of the effects of ionizing particles on the conductivity of single crystals by van Heerden7) in 1946 started what proved to be a very important field in the detection of nuclear radiations. Compared to the gas counters widely used at that time these solid counters offered higher stopping power, lower resolving time and a factor of about ten increase in the number of secondary electrons produced.

The first investigations were concerned with insulating crystals in order that a charge collection field could be maintained. Much work was devoted to the discovery of new crystals in which the effect could be observed. In spite of the large number of materials found which worked, the performance of the solid counters was poor. The energy resolution obtainable was worse than that of gas-filled counters. This was due primarily to the impurities in the crystals which reduce the lifetime of the mobile charge carriers and lead to incomplete charge collection. In addition, the pulse height produced by an incident particle of given energy was dependent on the previous counting history of the detector. This was due to the immobility of the positive ions in insulators which causes a space charge to be built up in the crystal.

In 1949 McKay8) reported the detection of alpha particles using a reverse biased germanium diode, although the signal-to-noise ratio obtained corresponds to a resolution of about 1 MeV. Subsequent work at the Oak Ridge National Laboratory[9)] started an intensive development of silicon and germanium diode detectors. The main lines of improvement have been in increasing the resolution and sensitive volume obtainable.

In this chapter, we will discuss the basic properties of the silicon detectors involved in the detection of ionizing radiations. We will discuss in some detail the response of these detectors to electrons.

## ii) The Detection Mechanisms in Solid State Detectors

The detection of ionizing radiations by solid state detectors depends on the production of mobile electron-hole pairs in the crystal. In semi-conductors the conduction band lies about one electron volt above the valence band, hence only a small amount of energy is required to produce an electron-hole pair. In silicon the incident particle expends an average of 3.6 eV per ion-hole pair produced.

These mobile carriers are collected on the diode capacitance by the electric field which exists in the depletion layer of a reverse biased diode. A typical arrangement of such a diode is shown in Fig. 1. The body of the diode is p-type silicon with an ohmic contact on the back. A thin $n^+$ region on the front is made by diffusing a donor, phosphorous[10)] or boron[11)], into the p-type silicon. Surface barrier junctions[12)] have also been used in these applications. Finally, a thin ohmic contact, usually gold, is

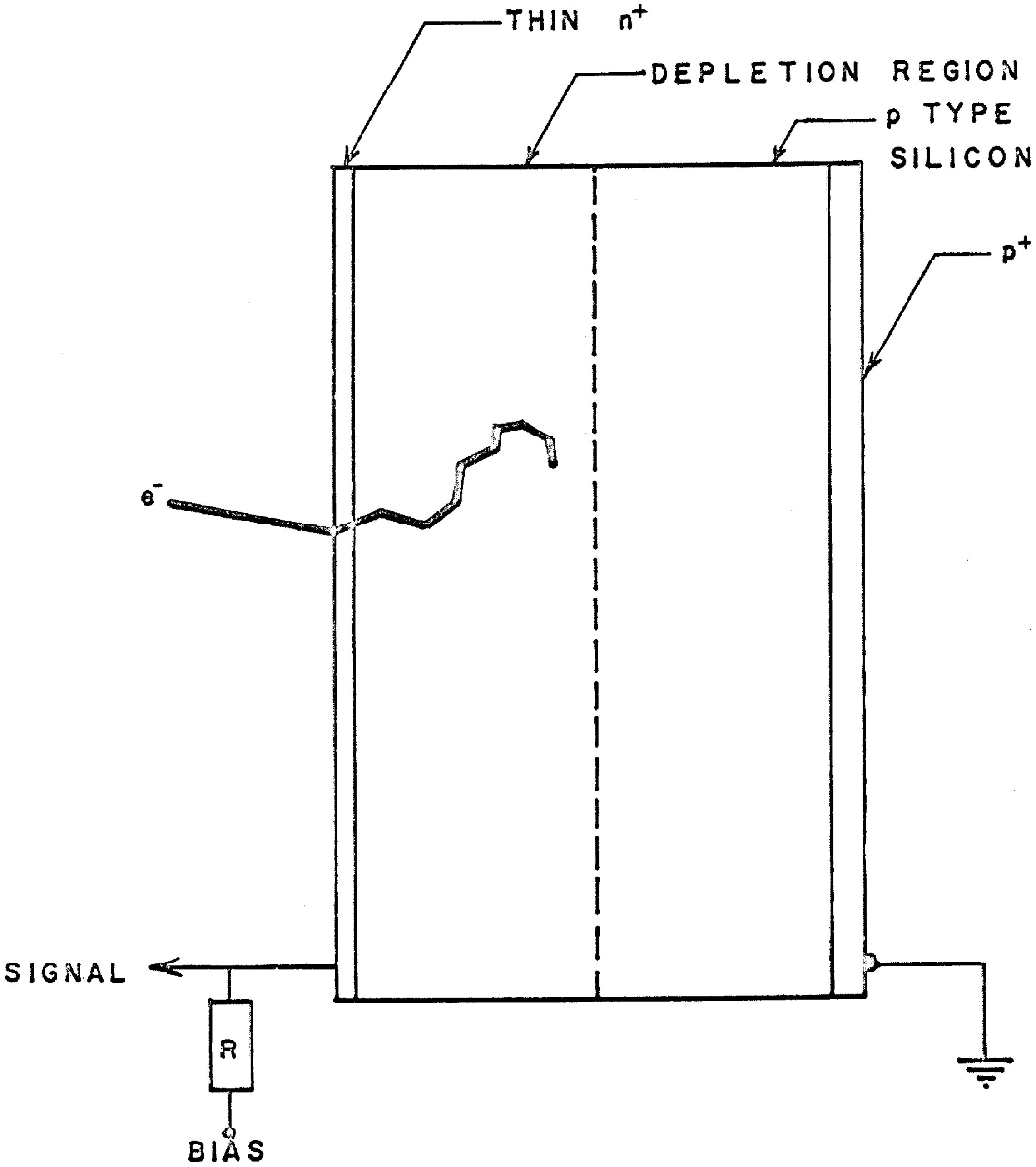

Figure 1

Solid State Diode Detector - Schematic

evaporated onto the front surface. It is important that the ohmic contact and the $n^+$ region be thin, as these regions have no collection field and hence are insensitive. In practice these regions are of the order of 20 μg/cm$^2$ thick. In the p-n type junction the depletion depth is proportional to $\sqrt{\rho(V + V_a)}$ where ρ is the resistivity and V is the applied reverse bias, and $V_a$ is the contact potential. Using large bias voltage to obtain large depletion depths has the disadvantage of decreasing the resolution obtainable with these counters. A method of lithium drift compensation[13)] has been used to increase the effective ρ. These lithium drifted counters can have depletion depths of several millimeters.

a) Energy Loss by Fast Electrons

For electrons with energy below about 5 MeV the most important processes leading to energy loss are the ionization of electrons into the conduction band and excitation. Only the first process contributes to the number of ion-hole pairs produced by the primary electron. Except for very low energy primary electrons, for which collisions must be considered as with the atom as a whole, we can consider collisions to occur with free electrons. Bethe[14)] has computed the energy loss per unit path length under these conditions to be

$$- \frac{dE}{dx} = \frac{4\pi e^4 NZ}{mv^2} B \qquad (1)$$

where Z is the atomic number of the absorbing material, e is the electronic charge, m is the mass of the electron, v is its velocity, N is the number of absorber atoms per cm$^3$ and B is the stopping number. For v << c, the velocity of light, Bethe[15)] gives the following expression for B

$$B = \log(0.583 \frac{mv^2}{I}) \tag{2}$$

where I is the mean ionization potential of the absorber. For higher energies B is given by Møller[16)] as

$$2B = \log\left[\frac{mv^2E}{2I}(1 - \beta^2)\right] - [\log 2][2\sqrt{1 - \beta^2} - 1 + \beta^2] + 1 - \beta^2 \tag{3}$$

where $\beta = v/c$. Figure 2 shows the rate of energy loss for electrons in silicon.

b. Gamma Radiation

For gamma rays below 5 MeV the important interactions with matter are via the photoelectric effect and Compton scattering. In the case of a beam of gamma rays, the interaction results in an exponential attenuation of the beam with a length $\ell^{-1} = \ell^{-1}_{\text{photo}} + \ell^{-1}_{\text{compton}}$ characteristic of the absorbing material. For energies below about 50 keV the photoelectric absorption length is the smaller in silicon. Heitler[17)] gives the following expression for the k-shell absorption length above the k-edge

$$\ell_{\text{photo}}^{-1} = \sigma_T \frac{NZ^5}{\alpha^4} 4\sqrt{2}\left(\frac{m}{k}\right)^{7/2} \tag{4}$$

where $\sigma_T$ is the Thompson scattering cross-section, $\alpha$ is the fine structure constant and k is the energy of the photon. In this process the photon is replaced by an electron of energy $E = E_\gamma - E_k$, where $E_k$ is the k-shell binding energy.

For energies above 100 keV the smaller absorption length is due to

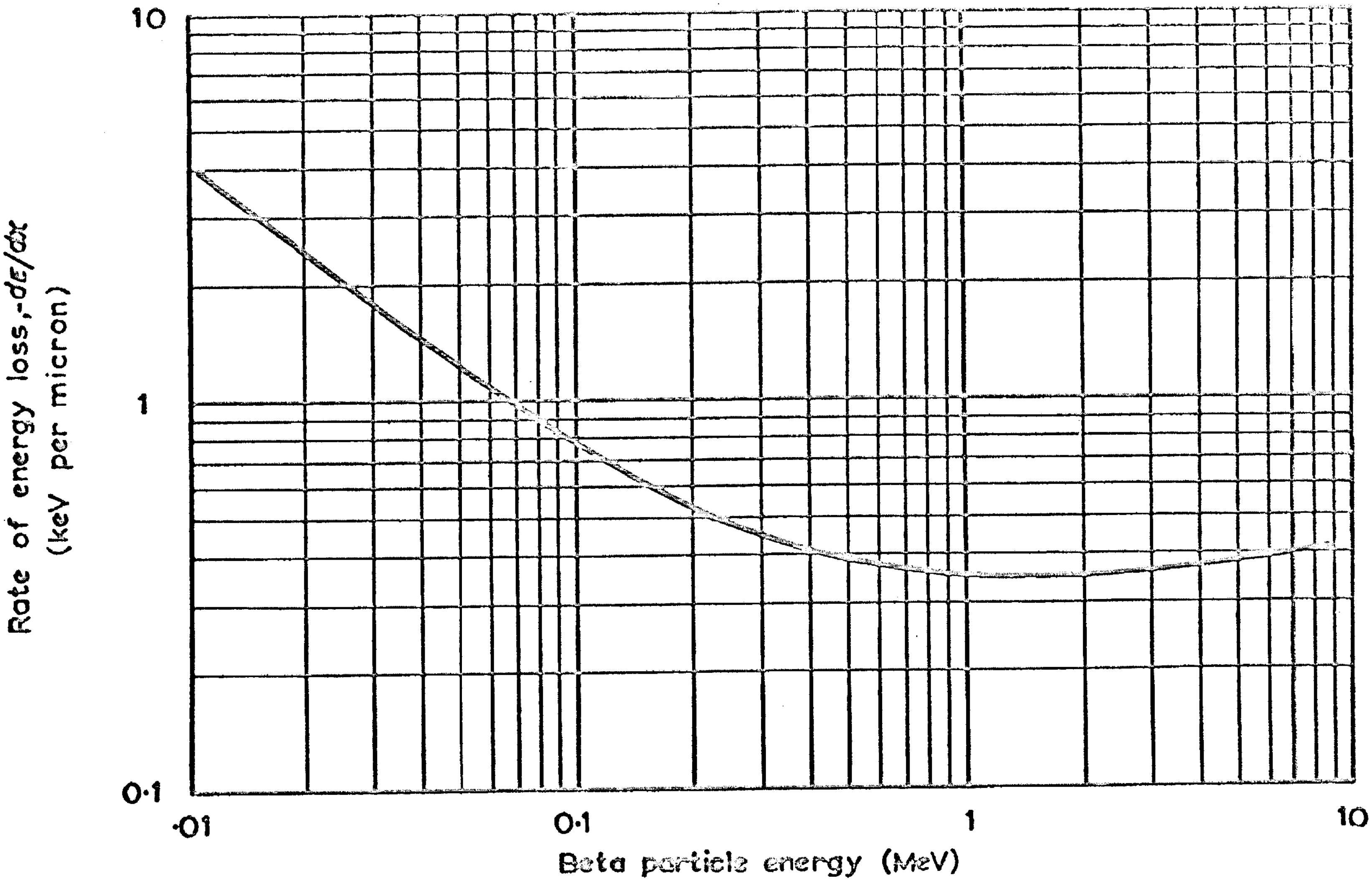

Figure 2

dE/dx for electrons in silicon. G. Dearnaley, Semiconductor Counters for Nuclear Radiation, Wiley (New York, 1963).

Compton collisions. The gamma rays scatter from atomic electrons which can be considered to be free. If the scattered gamma ray emerges at an angle of $\theta$ with respect to the initial gamma ray, its energy is given by

$$E'_\gamma = \frac{E_\gamma}{1 + \alpha(1 - \cos\theta)} \tag{5}$$

while the electron acquires an energy

$$E = E_\gamma - E'_\gamma \tag{6}$$

Here $\alpha = E_\gamma/mc^2$. The differential cross-section for Compton scattering of unpolarized gamma rays is given by Klein and Nishina$^{18)}$ as

$$\frac{d\sigma_c}{d\Omega} = \frac{r_0^2}{2}\left(\frac{E'_\gamma}{E_\gamma}\right)^2\left(\frac{E_\gamma}{E'_\gamma} + \frac{E'_\gamma}{E_\gamma} - \sin^2\theta\right) \tag{7}$$

where $r_0$ is the classical radius of the electron. The distribution in energy loss of the original gamma ray can be obtained by multiplying by the derivative of the angle $\theta$ with respect to the electron energy. The result is

$$\frac{d\sigma}{dE} = \left(\frac{d\sigma_c}{d\Omega}\right)\cdot\frac{\pi^2}{\alpha^2 mc^2}\left[\frac{(1+\alpha)^2 - \alpha^2\cos^2\varphi}{(1+\alpha)^2 - \alpha(2 + \alpha\cos^2\varphi)}\right] \tag{8}$$

where $\varphi$ is the angle between the incident gamma ray and the velocity of the Compton electron. This cross-section is shown in Fig. 3 for a number of different energies of the incident gamma ray.

Finally, we obtain the Compton absorption length by multiplying Eq. (8) by $(1 - E'_\gamma/E_\gamma)$, which is the energy removed per collision, integrating over angles and multiplying the result by NZ.

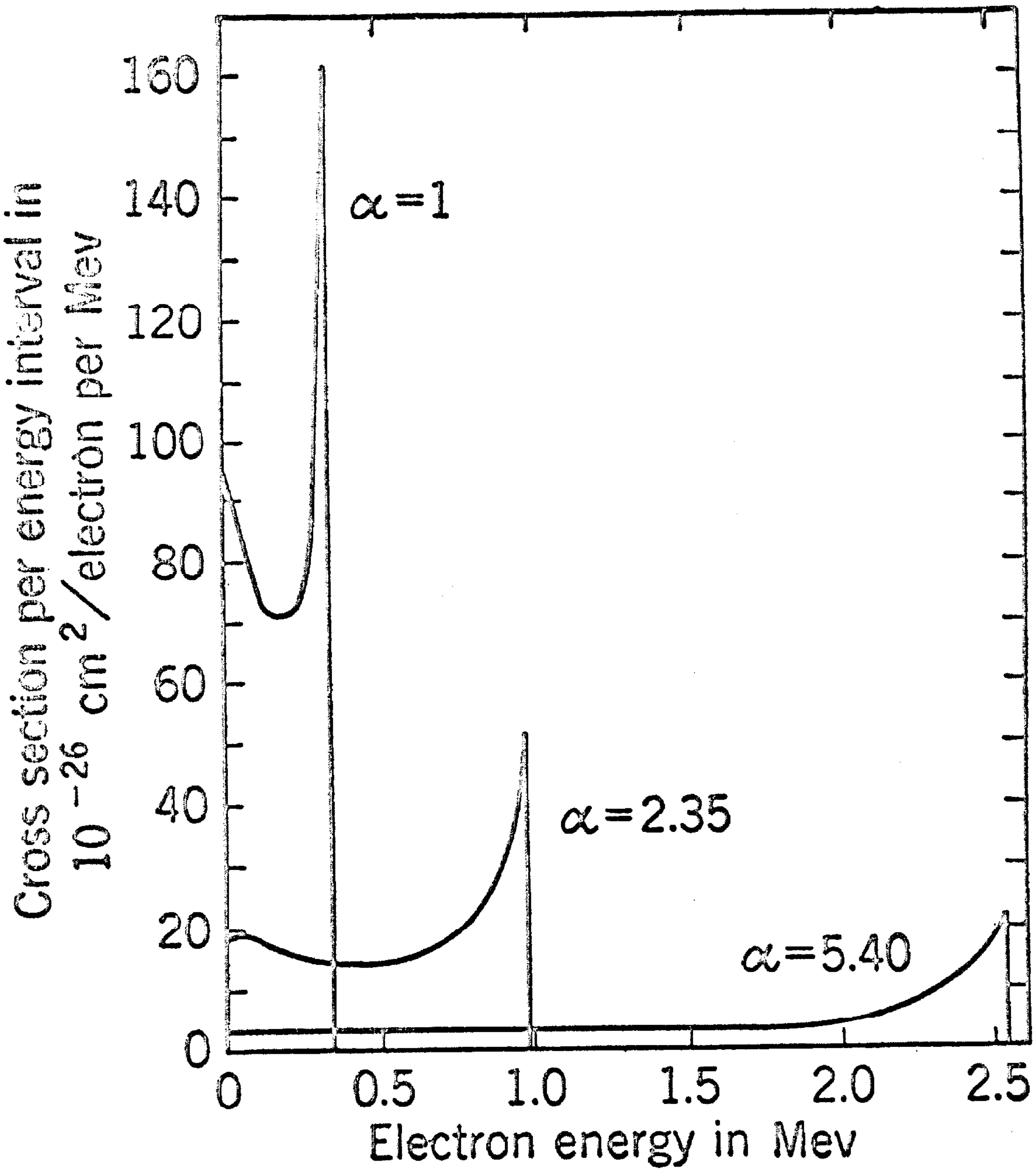

Figure 3

Energy distribution of Compton electrons for various energies of the incident gamma ray. Here $\alpha = E_\gamma/mc^2$, from Davidson and Evans, Rev. Mod. Phys. 24, 79 (1952).

$$\ell_{\mathrm{Compton}}^{-1} = 2\pi\, r_0^{\,2} NZ \left[ \frac{2(1+\alpha)^2}{\alpha^2(1+2\alpha)} - \frac{1+3\alpha}{(1+2\alpha)^2} - \frac{(1+\alpha)(2\alpha^2 - 2\alpha - 1}{\alpha^2(1+2\alpha)^2} \right.$$

$$\left. - \frac{4\alpha^2}{3(1+2\alpha)^3} - \left( \frac{1+\alpha}{\alpha 3} - \frac{1}{2\alpha} + \frac{1}{2\alpha^3} \right) \log\, (1+2\alpha) \right] . \qquad (9)$$

Figure 4 shows the total absorption coefficient for silicon along with the photoelectric and Compton absorption coefficients.

### c. Discussion

For the detection of electrons silicon is the most widely used detector material. The feasibility of producing lithium-drifted silicon detectors with large sensitive volumes makes it unnecessary to take advantage of the higher stopping power of higher Z materials such as germanium, since the higher leakage currents and thermal noise make the operation of these detectors more difficult. For gamma rays, however, the photo-absorption is proportional to $Z^5$ and the resulting increase in the total photo-absorption efficiency is a factor of about 30.

We list in Table 1 some of the relevant properties of intrinsic silicon and germanium.

## iii) Backscattering of Electrons

The backscattering of electrons from the surface of solids plays an important role in the determination of the response of solid state detectors to electrons. This problem has been considered by Bethe19) and Archard20), using a very simple model. They describe

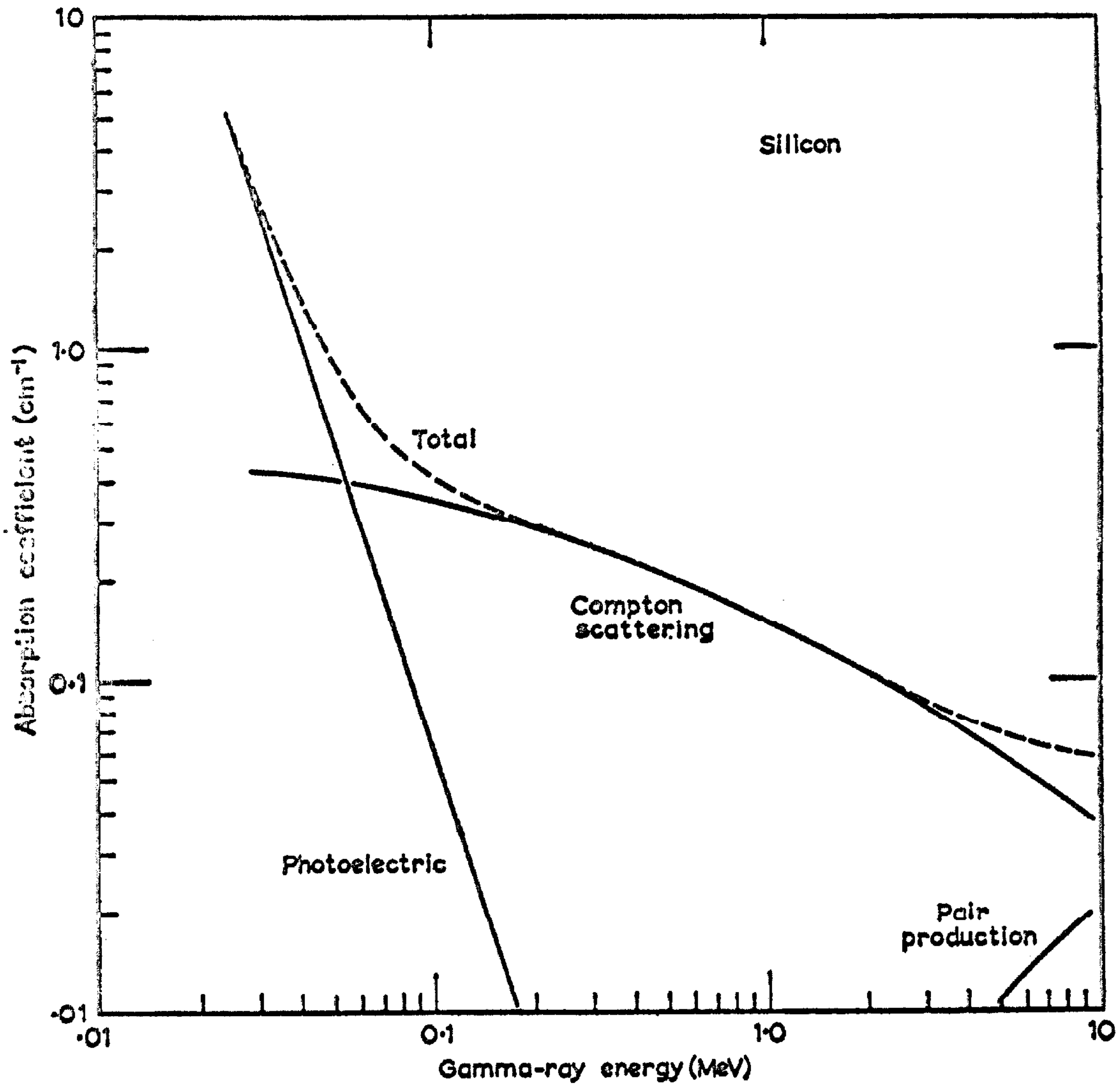

Figure 4

Gamma ray absorption coefficient for silicon, from G. Dearnaley, Semiconductor Counters for Nuclear Radiation, Wiley (New York, 1963).

TABLE 1

| Property | Silicon | Germanium |
|---|---|---|
| Atomic Number | 14 | 32 |
| Density | 2.33 $gm/cm^3$ | 5.33 $gm/cm^3$ |
| Atoms per $cm^3$ | $4.96 \times 10^{22}$ | $4.41 \times 10^{22}$ |
| Dielectric constant | 12 | 6 |
| Energy Gap | 1.106 eV | 0.75 eV |
| Intrinsic Resistivity (300°C) | 230,000 $\Omega$ cm | 47 $\Omega$ cm |
| Intrinsic Carrier Conc. (300°C) | $1.5 \times 10^{10}/cm^3$ | $2.35 \times 10^{10}/cm^3$ |
| Electron Mobility (300°C) | 1350 $cm^2$/volt-sec | 3800 $cm^2$/volt-sec |
| Hole Mobility (300°) | 480 $cm^2$/volt-sec | 1800 $cm^2$/volt-sec |
| Electron Diffusion Const. (300°C) | 35 $cm^2$/sec | 92 $cm^2$/sec |
| Hole Diffusion Const. (300°) | 12.4 $cm^2$/sec | 44 $cm^2$/sec |

Some properties of intrinsic silicon and germanium the backscattering by considering the electrons to penetrate to a depth of "complete diffusion" $x_d$, and then to diffuse uniformly in all directions from this point. The exact definition of $x_d$ is a matter of defining what is meant by the depth of complete diffusion. Bethe defines $x_d$ to be the depth at which the average deflection of the electron path is $68.4^\circ$ (the average cosine of the deflection angle is 1/e). He then obtains the approximate result $x_d/x_r \simeq 6/Z$, where $x_r$ is the range of the electrons in the solid. The backscattering coefficient R is defined as the total number of electrons which leave the solid in the backwards direction. In this theory R is given by the fraction of a sphere of radius equal to $(x_r - x_d)$ which extends beyond the surface of the solid. The result for the coefficient R is

$$R = \frac{1}{2}\left(1 - 2\frac{x_d}{x_r}\right) / \left(1 - \frac{x_d}{x_r}\right) . \tag{10}$$

It will be convenient later to use the quantity S = 1 - R, which is the fraction of the electrons which stop in the solid.

The most important feature of this theory is that S is independent of the incident energy of the electrons. The energy distribution of the backscattered electrons would be essentially constant up to the energy corresponding to $(x_r - 2x_d)$ above which it would decrease. However, this theory neglects the large angle scatterings and surface effects which tend to make the distribution of backscattered electrons constant.

## III. DETECTOR RESOLUTION AND ELECTRONICS

### i) Resolution

In this chapter we describe some of the factors which contribute to the resolution of solid state detectors. The finite resolution is due partly to the statistical nature of the production of ion-hole pairs in the counter and partly to the electrical noise of the counter and its associated electronics. The deviations which result have a Gaussian distribution. We will be interested in finding the standard deviation of the distribution for each factor considered. In the subsequent applications we will always be interested in the spread in the pulse amplitudes which we record as a result of an ionizing particle being completely stopped in the detector. It is convenient, therefore, to express these deviations in terms of the energy a particle would have to deposit in the detector in order to produce a pulse equal to this deviation.

We can obtain an expression for the contribution due to the statistical fluctuations in the number of ion-hole pairs produced by an ionizing particle if for the moment we consider the ionizing events to be independent. Then the standard deviation in this number, N, is just $\sqrt{N}$ if N is large. The number of ionizing events is

$$N = \frac{E}{w} \qquad (11)$$

where w is the mean energy required to produce an ion-hole pair and E is the energy of the particle. Therefore, the standard deviation due to this factor is

$$\sigma_{\text{stat}} = w\sqrt{N} = \sqrt{wE}. \tag{12}$$

This number determines the ultimate limit to the resolution obtainable.

In the analysis above correlations between the ionizing events have been neglected. The correlations arise from the fact that the total energy loss due to all the ionizing events must equal the initial energy of the incident particle. The effect of these correlations has been investigated by Fano[21)]. The result is that $\sigma$ should be multiplied by a Fano factor F, which is a function of the absorber material. Measurements by Blankenship[22)] indicate that the Fano factor may be as small as 0.5 for silicon.

Electronic noise generated in the detector is due mainly to thermal or Johnson noise and to shot noise. The expression for the Johnson noise is contained in Appendix IV. By cooling the detector to liquid nitrogen temperature the thermal noise can be reduced to below 1 keV. Shot noise depends on the current drawn by the detector, including bulk leakage currents and surface currents. In good detectors this also contributes less than 1 keV to the noise width.

The most important source of noise is in the electronics associated with the detectors. This contribution generally determines the total noise width of the system. If the first stage of amplification has a large gain we need only consider the noise contribution due to this stage. In Appendix IV we list the individual contributions to the total noise referred to the input of the amplifier. Adding these contributions we obtain for the total noise width

$$(\sigma_{tot})^2 = \left(\frac{w}{e}\right)^2 \left[\left(\frac{e\,I_d}{2} + \frac{kT}{2R_g}\right)\tau + \frac{2.5}{g_m} \cdot \frac{kT_e}{2} \cdot \frac{C_{in}^2}{\tau} + \frac{A_f}{2}\,C_{in}^2\right]. \tag{13}$$

Figure 5 shows $(\sigma_{tot})^2$ as a function of $\tau$ for various values of $I_d$. $\sigma_{tot}$ has a minimum where the contribution due to shot noise is equal to the contribution due to leakage currents. The value of this minimum is an increasing function of $C_{in}$.

### ii) Electronics

The electronics associated with each detector is shown in Fig. 6a. The low noise preamplifier used was an Ortec Model 109 FET amplifier. In order to minimize the input capacitance, the detector was connected directly to the gate of the field effect transistor via a decoupling capacitor. The preamplifier had an integrating time constant of 40 nsec and a differentiating time constant of 400 µsec. The post amplifier was an Ortec Model 410 Multimode Amplifier with variable gain and variable integrating and differentiating time constants. The time constants used in the experiments were 1 µsec. The apparatus for the coincidence measurements is shown in Fig. 6b. The spectra were recorded in a Nuclear Data 1024 channel two-parameter analyzer.

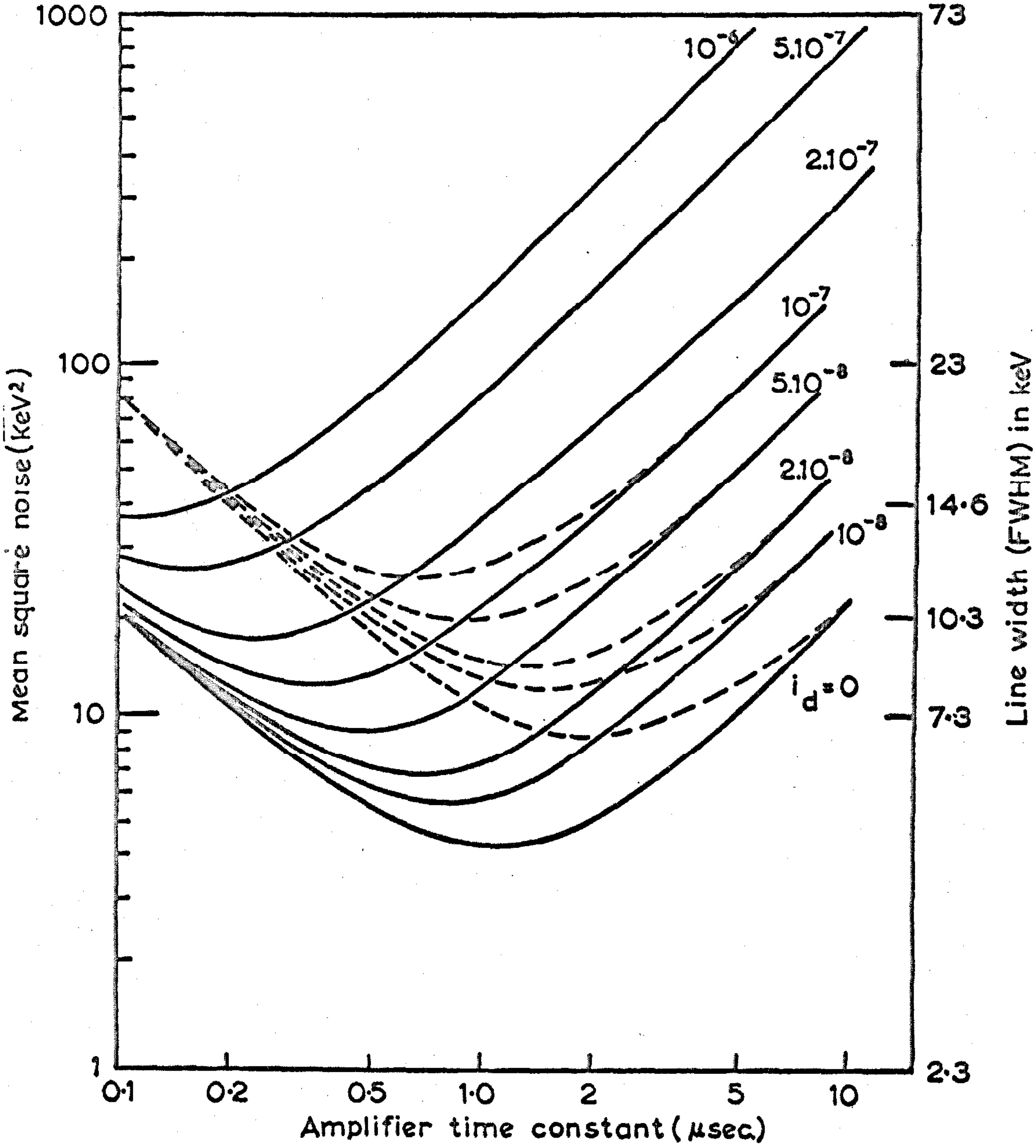

Figure 5

Noise width as a function of amplifier time constants for various input current $I_d$. The solid lines are for $C_{in}$ = 40 pf, the dotted lines for $C_{in}$ = 80 pf. From F.S. Goulding and W.L. Hansen, Nucl. Instr. & Meths. 12, 249 (1961).

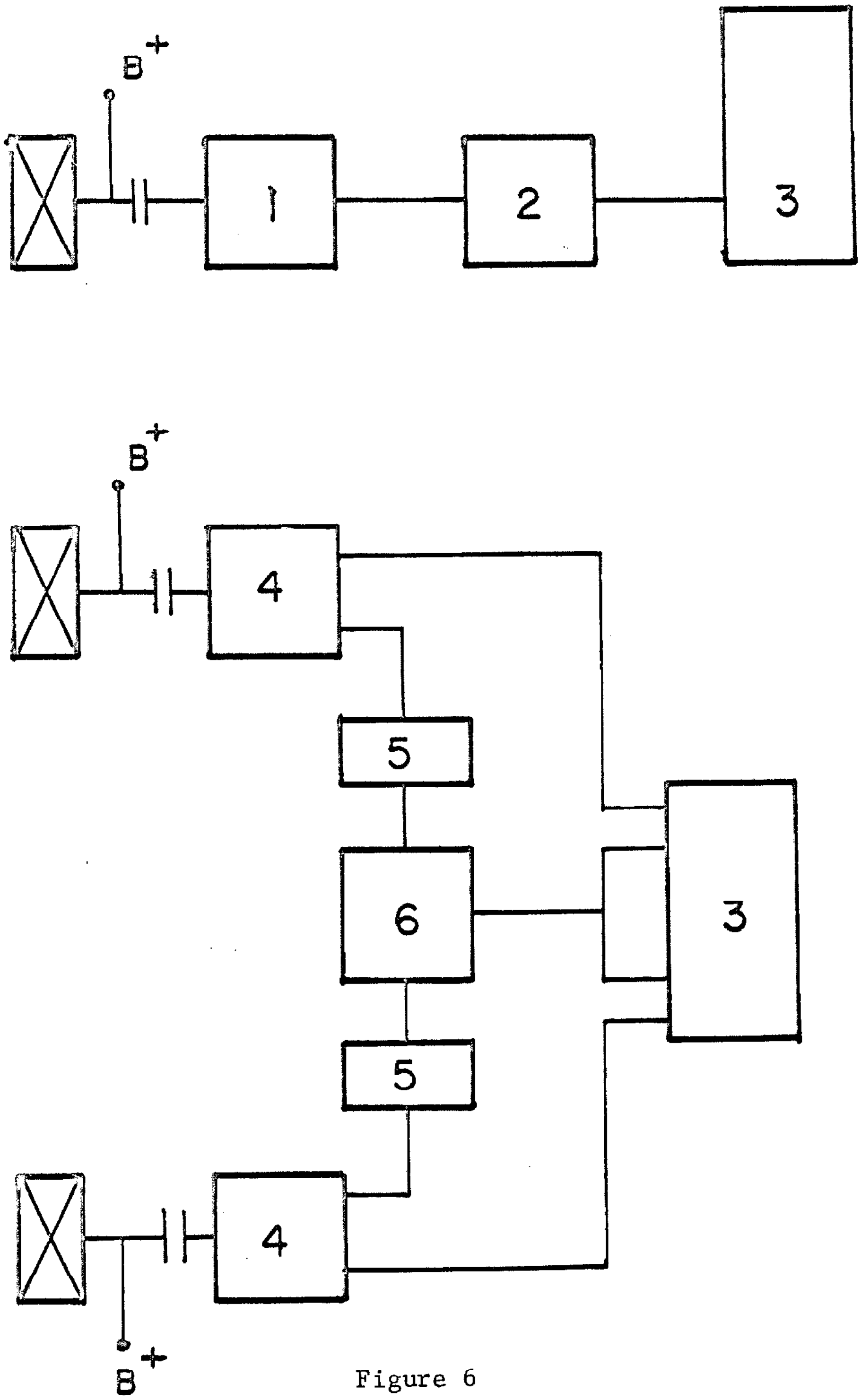

Figure 6

a) Electronics associated with solid state detector. 1 - Low noise preamp, 2 - Main amplifier, 3 - Pulse height analyzer.

b) Electronics used in coincidence measurements. 4 - Preamp and main amplifier, 5 - Single channel integral - differential discriminator, 6 - Coincidence unit with $2\tau = .1$ μsec.

## IV. EXPERIMENTS WITH A SINGLE DETECTOR

The experiments to be described in this chapter were performed to determine the response function for a single detector. It is known that the backscattering from solids is independent of energy and the energy distribution is relatively flat. These experiments were designed to determine the amount of backscattering in the experimental conditions to be used, and to gain an understanding of the importance of the environmental effects.

### i) Spectrometer Illumination

The most direct determination of the detector response was accomplished by using the detector in conjunction with a magnetic spectrometer. By this technique we are able to illuminate the detector with a thin beam of mono-energetic electrons perpendicular to the sensitive surface of the detector. The small amount of scattering in the spectrometer has a negligible effect on the results obtained. Using this arrangement, the general shape of the pulse-height spectrum was a full energy peak and a low energy tail, the tail being essentially flat (Fig. 7). The peak shows no discernible deviation from the expected Gaussian shape. This means that the energy loss in the dead layer is much less than the resolution, which is about 40 keV in these experiments. For incident energies below the range of the detectors the integrated area under the low energy tail is about 20 percent of the total area, independent of the primary electron energy. This is consistent with previous measurements of the backscattering coefficient for

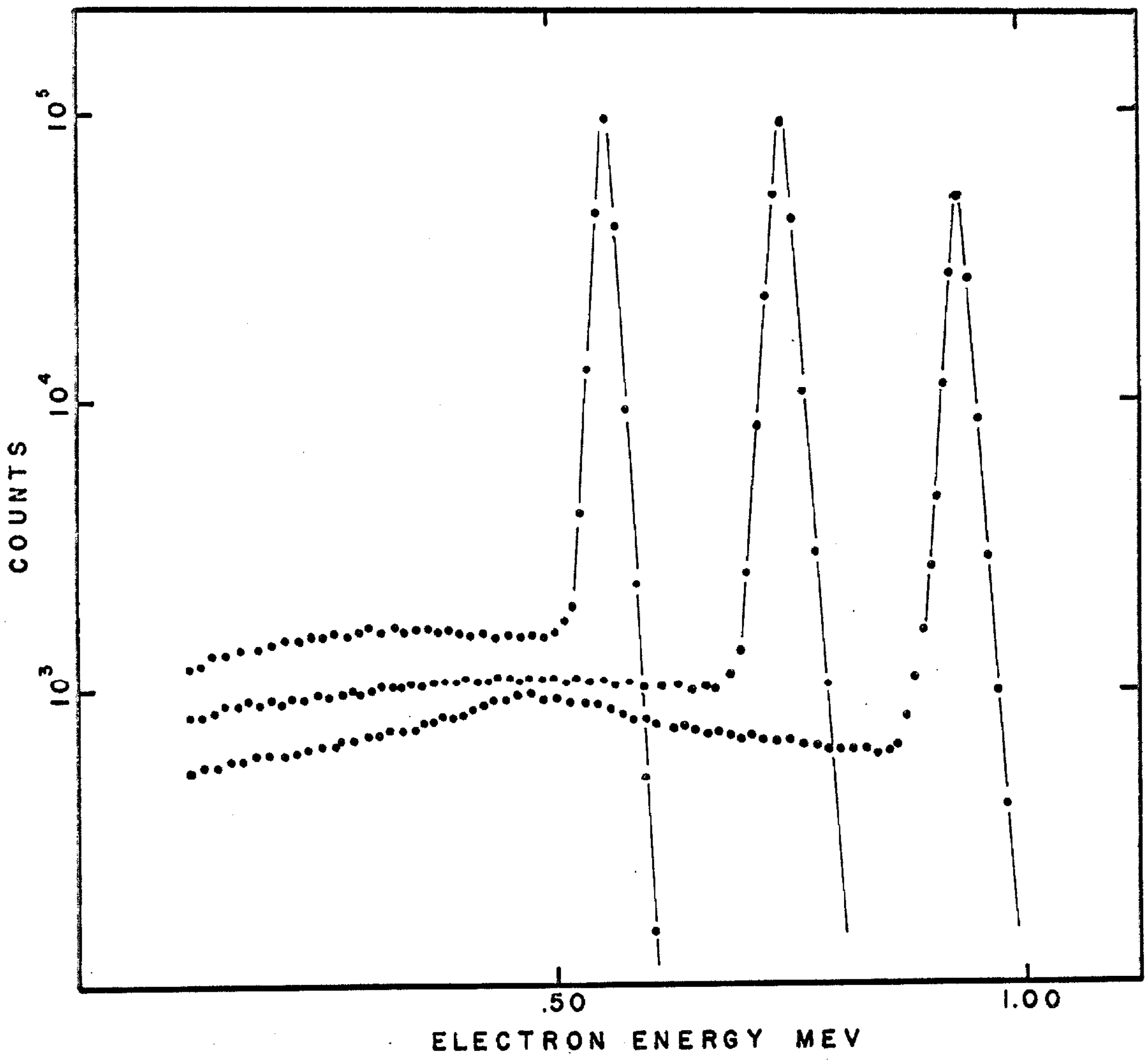

Figure 7

Pulse height spectrum obtained by illuminating a 0.7 $cm^2$ by 1 mm deep detector with mono-energetic electrons from a magnetic spectrometer. The thickness of the detector corresponds to about 700 keV. The curves are normalized to constant area.

silicon[23,24]. As the energy is increased beyond the range of the detector, the fraction of counts in the low energy tail increases. In addition, the energy distribution is no longer flat, a broad minimum ionization peak appearing at the energy corresponding to the thickness of the detector[25].

### ii) Shape Measurements with the Single Detector

In order to measure the shapes of beta spectra with this arrangement it is necessary to have a much better determination of the detector response than is possible using the technique described above. The qualitative information obtained from the experiments with mono-energetic electrons was used to obtain a reasonable functional form for the response function. This was taken to be a $\delta$-function of amplitude S at the energy of the incident electron plus a constant low energy tail. The integral of the response function is normalized to unity. This response function is to be folded with a Gaussian whose second moment is appropriate to the resolution of the instrument. This is determined by measuring the width of the photo peaks of $Co^{60}$ and $Sc^{46}$ gamma rays. In the case of a slowly varying continuous distribution the instrumental resolution distorts the spectrum only slightly and was accounted for by the method described in Appendix I.

The parameter S was determined by measuring the beta spectrum of $P^{32}$. Using the values for S thus obtained, the shape factors of the beta spectra of $Bi^{210}$ and $Pr^{143}$ were determined.

a) <u>Sources</u>

The nuclei used in these experiments all decay essentially 100 percent by beta emission to the ground state. The decay of $Bi^{210}$ is complicated somewhat in that it decays to $Po^{210}$ which in turn decays by $\alpha$-emission with a half-life of 138 days. The effects due to the $\alpha$-decay can be eliminated by chemically separating the $Bi^{210}$ immediately before use, as described below.

<u>$P^{32}$</u>

$P^{32}$ has an endpoint energy of 1.712 MeV and a half-life of 14 days. The phosphorous was obtained commercially carrier free as phosphoric acid. The sources contained impurities of $P^{33}$ which beta decays with an endpoint energy of 250 keV. Sources were prepared by evaporating the acid to dryness on 0.5 mg/cm$^2$ mylar foils.

<u>$Bi^{210}$</u>

$Bi^{210}$ has an endpoint energy of 1.06 MeV and a half-life of 5 days. Carrier free bismuth was obtained by chemical separation from commercially obtained $Pb^{210}$. The $Pb^{210}$ was placed on an ion exchange column containing Dowex-50 resin. Bismuth and lead were eluted from the column with $2NHNO_3$ 26). The bismuth and lead were then placed on a Dowex -50 microcolumn and $Bi^{210}$ was eluted with 0.6 NHCl. The $Bi^{210}$ solution was then evaporated to dryness on a mylar backing.

$\underline{Pr^{143}}$

$Pr^{143}$ has a beta endpoint energy of 930 keV and a half-life of 13.8 days. $Pr^{143}$ was obtained by the reaction $Ce^{142}(n)\ Ce^{143} \xrightarrow{\beta} Pr^{143}$. The $Ce^{143}$ has a half-life of 33 hours. Carrier free sources of $Pr^{143}$ were prepared by extracting the cerium from a $10NHNO_3$ solution 27). The remaining $Pr^{143}$ was then precipitated with $Fe(OH)_3$ and the iron was removed by solvent extraction. The resulting aqueous solution of $Pr^{143}$ was evaporated to dryness on a mylar backing.

### b) Shape Measurements

The system response to a continuous beta spectrum I(E) can be written in terms of the parameter S, as described in Appendix I, as

$$O(E) = S(E)\ I(E) + \int_{E}^{E_0} \frac{(1 - S(E'))}{E'}\ I(E')\ dE' \qquad (14)$$

where O(E) is the observed spectrum and $E_0$ is the endpoint energy of the beta decay. Using the known shape factor of $P^{32}$ 28) for I(E), Eq. (14) can be solved for S(E) in the manner described in Appendix I. The result is shown in Fig. 11 .

Using the function S(E) obtained above, the shape factors of the beta spectra of $Bi^{210}$ and $Pr^{143}$ were determined by solving Eq. (14) for I(E). Figure 12 shows the function

$$C(W) = \frac{2\pi^3\ I(W)}{F_0(Z,W)pW(W_0 - W)^2 L_0(r_0)} \qquad (15)$$

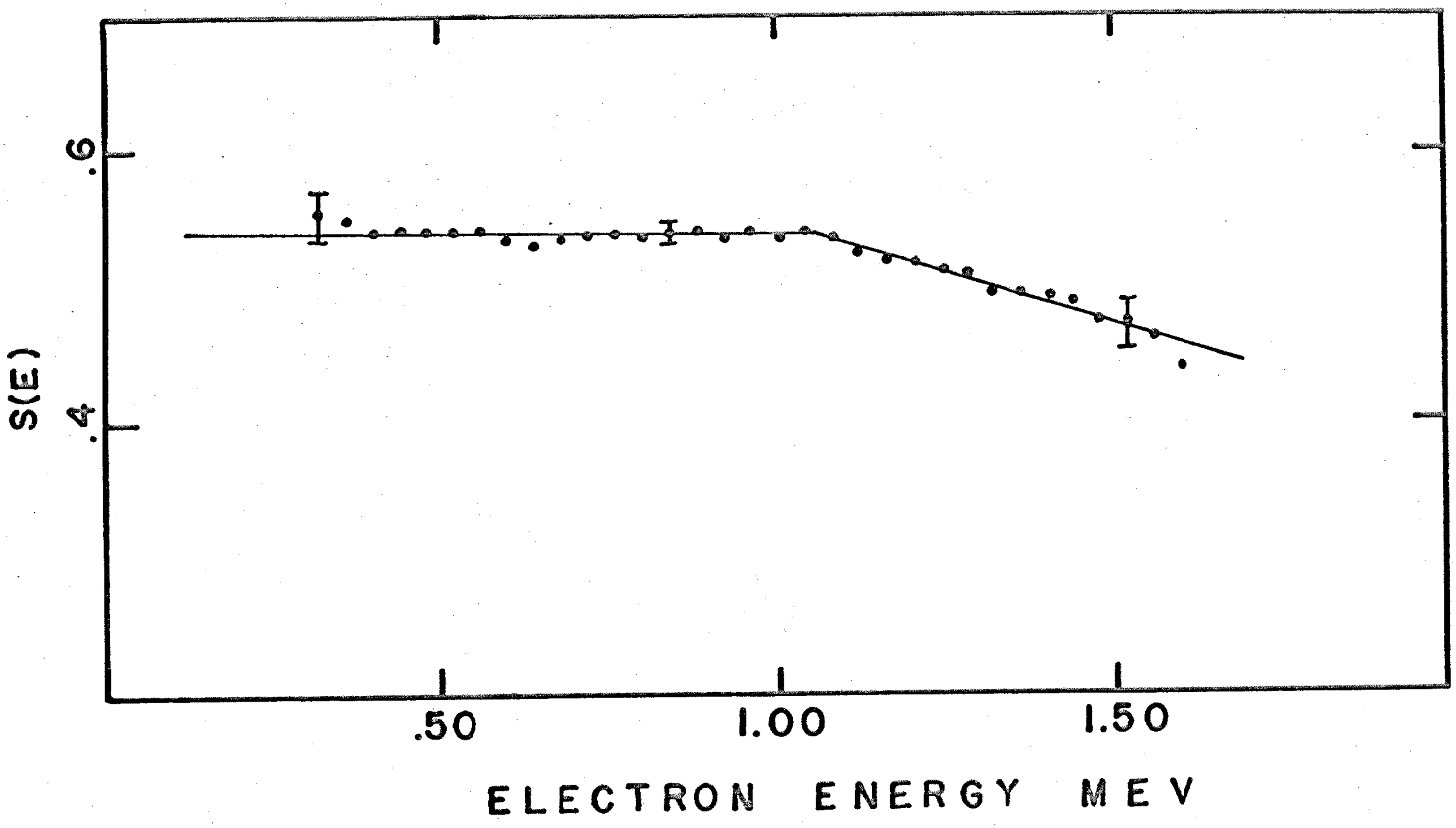

Figure 11

S(E) for a single detector obtained using the beta decay of $P^{32}$ as a standard spectrum. The solid line was the S(E) used to reduce the $Bi^{210}$ and $Pr^{143}$ data.

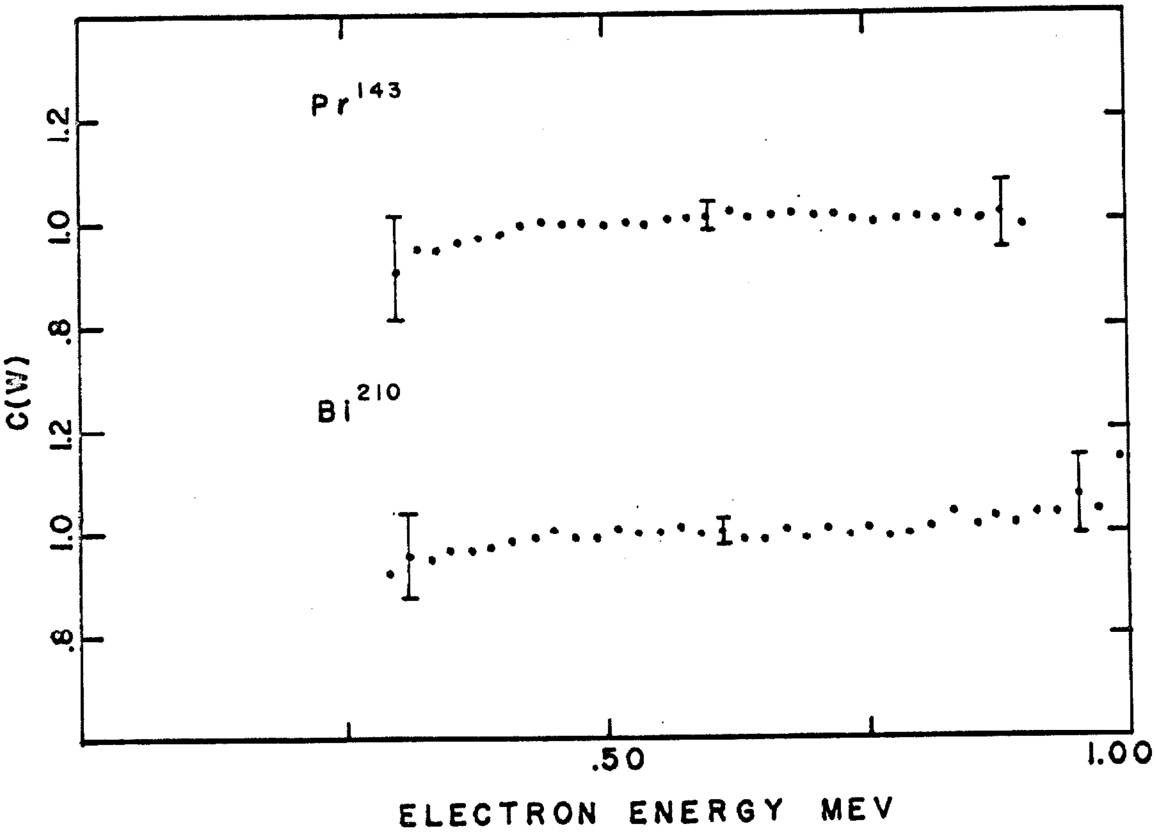

Figure 12

The shape factor C(W) for Bi$^{210}$ and Pr$^{143}$ obtained using a single detector. The beta decay of P$^{32}$ was used as a standard spectrum.

for $Bi^{210}$ and $Pr^{143}$. Here $F_0(Z,E)$ is the Fermi function defined by Bhalla and Rose[39)], p is the electron momentum and W is the total electron energy.

c) Discussion

Although the results obtained for the shape factors of the beta decays of $Bi^{210}$ and $Pr^{143}$ are consistent with previous work[30,31)], the accuracy with which these shape factors can be determined by this method is poor. As seen in Fig. 11 the function S(E) becomes as large as .54 and decreases slightly above 1.2 MeV. This causes the cumulative effect of the high energy electrons being scattered to lower energies to be large. In order to measure percent effects in the shape factor of a beta decay, S(E) must be determined to better than 1 percent, due to the fact that the second term in Eq. (14) becomes larger than the first term at low energies. This in turn means that the shape factor of the reference spectrum must be determined considerable better than 1 percent.

Another serious problem is the dependence of S(E) on the experimental environment. As indicated from the measurements with a single detector, there is a large amount of electron scattering in the vacuum chamber. This results in the function S(E) being dependent on the particular experiment and on the particular reference spectrum used.

## V. EXPERIMENTS WITH $4\pi$ DETECTORS

The serious distortions due to the backscattering of electrons from a single solid state detector can in principle be eliminated by imbedding the source in the detector and counting over the whole sphere. This method has been applied successfully to plastic scintillators. In the case of plastic scintillators, however, the relatively poor energy resolution obtainable makes the analysis of the data difficult.

In this chapter we discuss a $4\pi$ spectrometer using two lithium-drifted silicon detectors manufactured by Simtec Ltd. In this arrangement it is possible to achieve a $\delta$-function response to mono-energetic electrons and to take advantage of the high energy resolution obtainable with solid state detectors. Because of the totally different counting geometry there are new effects which can lead to spectral distortions.

The first effect concerns the energy loss in the source backings. In the case of the $4\pi$ spectrometer this can become serious because electrons which have been scattered out of one detector must pass through the source backing material. A single electron may make several such scatterings. At low energies the dE/dx for electrons becomes large. It is possible that these electrons may lose a considerable amount of energy. Secondly due to the finite separation of the detectors, there is some loss of solid angle. The relevant effect of the resulting imperfect $4\pi$ geometry in these experiments is the scattering of electrons from active to inactive regions, or from inactive to active regions of the detection system.

These electrons produce pulses smaller than would be recorded if they were stopped in the detector.

These effects have been studied experimentally and the shape factor of the beta decay of $P^{32}$ has been measured.

a) Experimental Apparatus

The experimental apparatus for the $4\pi$ detection system is shown in Fig. 13. The two detectors are mounted on thin-walled stainless steel tubes and pressed together by a weak spring. Each detector has an active volume 1.0 cm$^2$ by 3 mm deep. The source is placed on thin foils between the detectors. The entire system is then placed in a thin-walled stainless steel cryostat which is surrounded by a liquid nitrogen bath. The cooling of the detectors is accomplished by the use of an exchange gas in the cryostat. Dry helium is used as the exchange gas.

The detector signals were brought out via thin stainless steel wires connected to the gate of the input FET. Recording of spectra was done in two ways. To obtain single spectra the output currents of the two post amplifiers were added by a resistive network. The resulting sum pulses were then analyzed in a multichannel analyzer. To study the interaction of the two detectors, the coincident pulse height spectrum of the sum pulses and the singles pulses from one of the detectors were analyzed in a two parameter pulse height analyzer. In either case the gains in the two halves of the system were matched to better than 1/2 percent by using the photo-absorption peaks of the gamma lines of $Co^{60}$ and $Sc^{46}$. This also provides a means for energy calibration of the system and

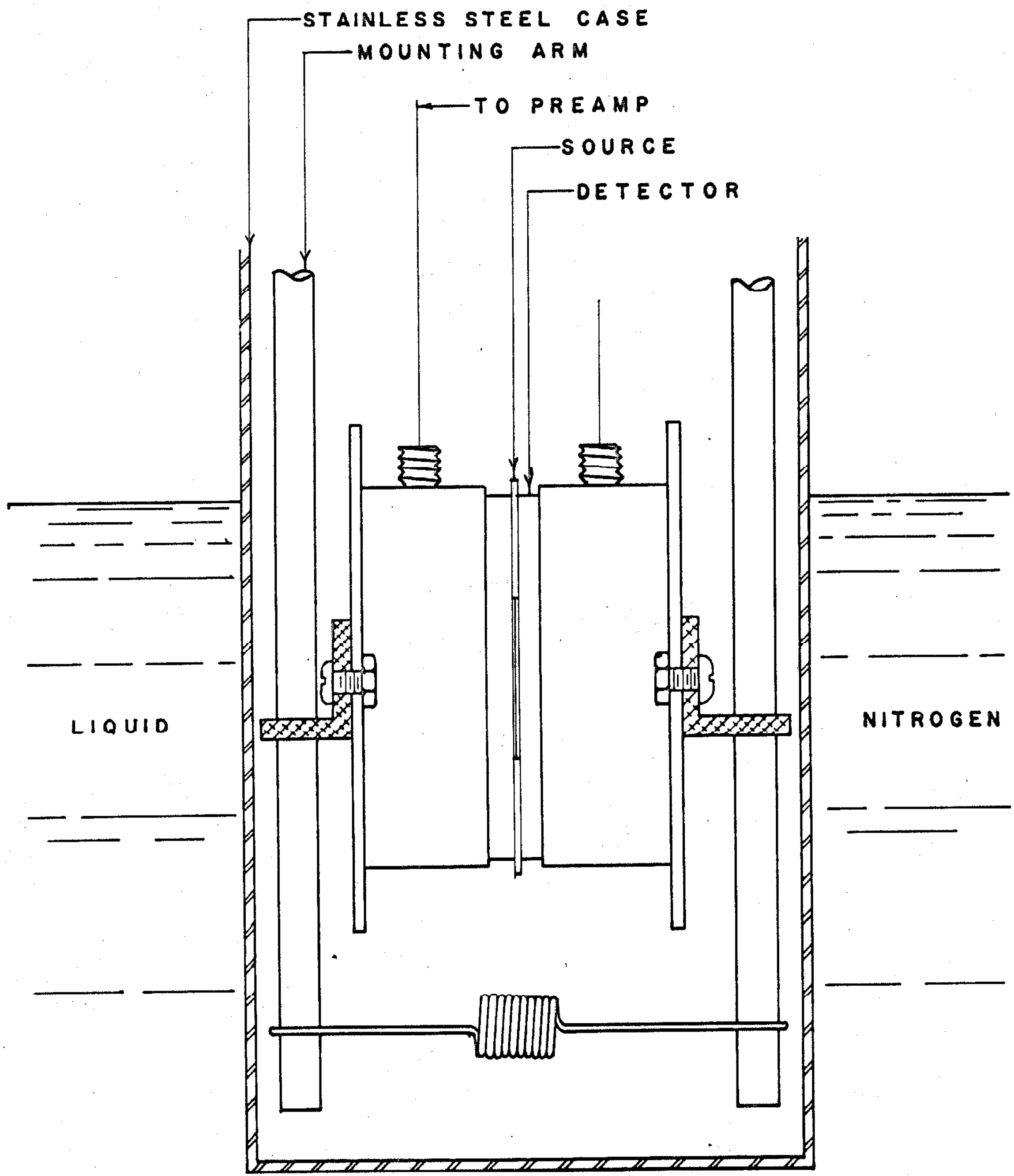

Figure 13

Apparatus for the 4π detectors. The cryostat is filled with dry helium which is used as an exchange gas to cool the detector.

determination of the system energy resolution. We may note that in the case of the singles spectrum it is generally not possible to sum directly the charges collected by the detectors because of small variations in the detectors themselves. These variations are due to variations in impurity concentrations and distributions in the silicon.

### b) Source Absorption

Because the lithium-drifted detectors required for the spectrometer were not available on an unlimited basis, we could not deposit sources directly onto the detector surface, as reported by Reynolds and Persson[32]. We chose to confine the sources between two Formvar films 15 $\mu g/cm^2$ thick.

In order to examine the effects due to electrons losing energy while traversing these films $Bi^{207}$ sources were prepared on mylar backings whose total thickness was 1 $mg/cm^2$. The two-dimensional pulse height spectrum of the sum pulses in coincidence with the singles spectrum in one of the detectors was recorded. In this way, the effect of low energy electrons passing through the foil can be observed. In Fig. 14 a contour plot of the region corresponding to the 1.06 MeV K-conversion electron sharing its total energy between the two detectors is shown. If there were no absorption in the backings the peak would lie along a line of constant sum energy equal to the energy of the K-conversion electron. It is seen that the peak falls below this line. Figure 15a shows profiles through this peak for various energies deposited in a single detector. Figure 15b shows the peak position as a function of the energy deposited in a single detector. The solid line is the dE/dx expected for electrons passing

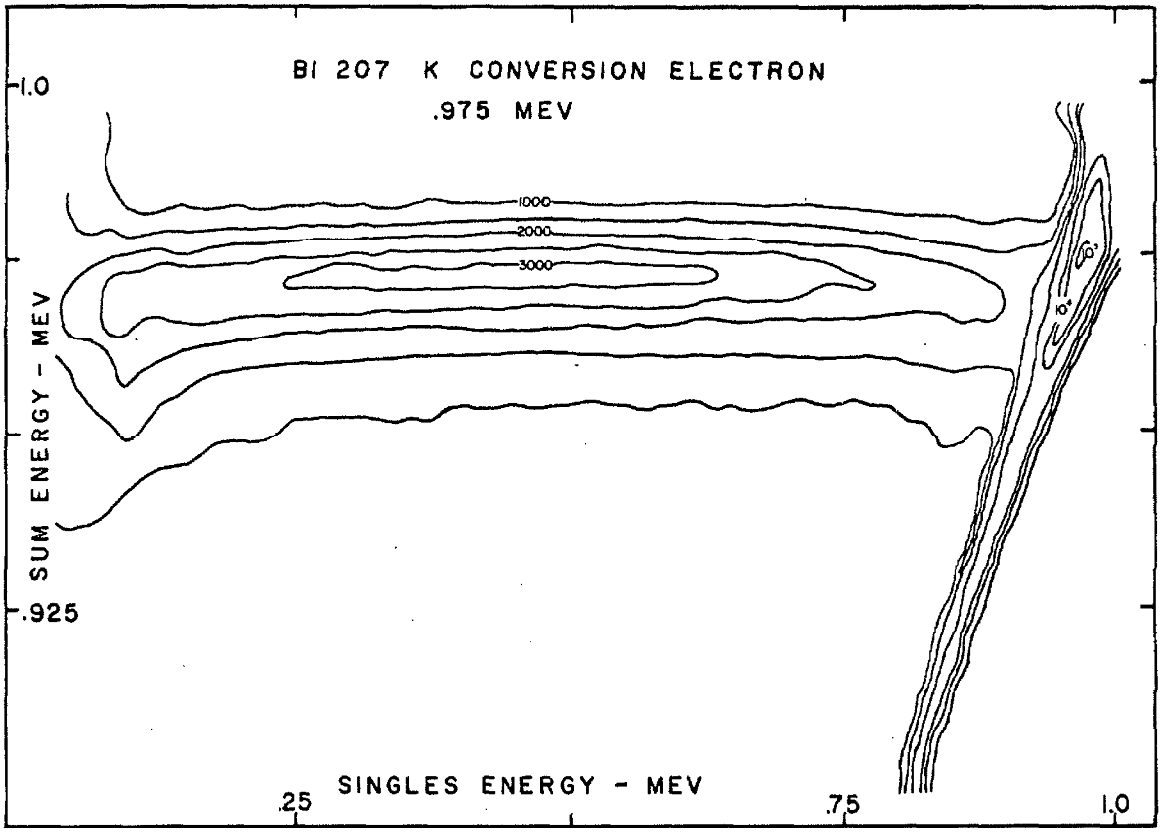

Figure 14

Contour plot of the sum pulses produced by the 975 keV conversion electron in $Bi^{207}$ in coincidence with the singles pulses in one of the detectors. Pulses that fall along lines of constant sum energy represent electrons which share their energy between the two detectors. The sources were mounted between $1mg/cm^2$ mylar foils.

FIG 15 a

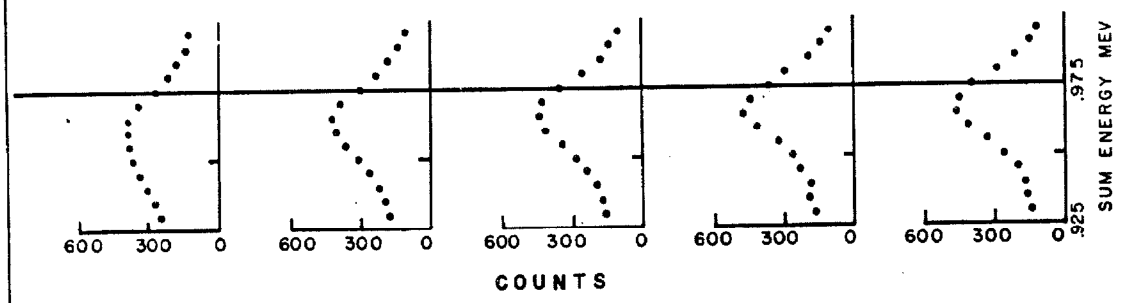

FIG 15 b

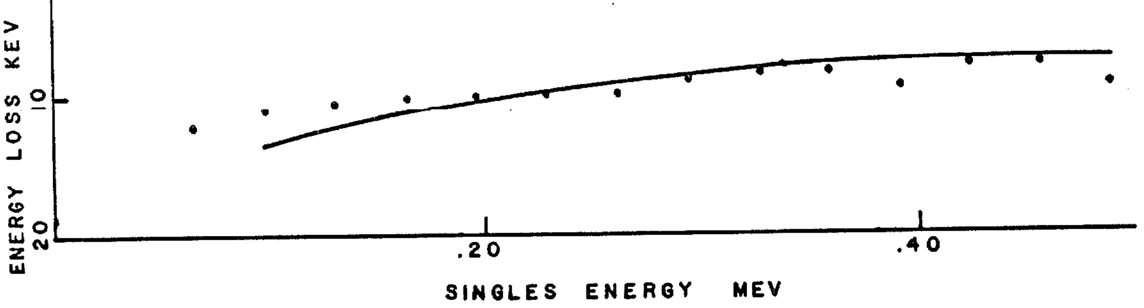

a)
Profiles through the contour plot at various singles energies. At low singles energies the tail becomes pronounced because the dE/dx becomes comparable to the electron energy.

b)
Peak position as a function of singles energy. The solid line is the dE/dx for electrons passing through 6 $mg/cm^2$ mylar.

through 6 mg of mylar. An electron which is scattered once through the backing must traverse 3 thicknesses of the mylar, and the average value of sec $\theta$, the angle at which it passes is about 2. Figure 16 shows a contour plot of the region around the K and L conversion peaks. The peaks are skewed slightly to the low energy side. A shoulder on the low energy side, due to backing thickness, extends 10 keV below the peak, which is roughly the effective thickness of the mylar backings.

These effects are eliminated by the use of thin Formvar backings. The 15 $\mu g/cm^2$ Formvar backings used during the shape measurements cause an energy loss of less than 100 eV for electrons whose energy is greater than 1 keV. Since the noise width of the combined system was 10 to 15 keV, this does not contribute appreciably to spectral distortions.

c) Detector Separation

The effect of the detector separation was determined by observing the change in the shape factor of a beta spectrum as a function of the distance between the detectors. For this purpose sources of $P^{32}$ were prepared on Formvar foils. The sum spectrum of the two detectors was recorded for a number of different spacings of the detectors. The sum spectra were fitted to the function

$$N(W)dW = \frac{1}{2\pi^3} F_0(Z,W)pW(W_0 - W)^2 L_0(r_0)C(E)dW \qquad (16)$$

in the manner described in Appendix I. C(E) was taken to be

$$C(E) = k(1 + AE + B/E) \; . \qquad (17)$$

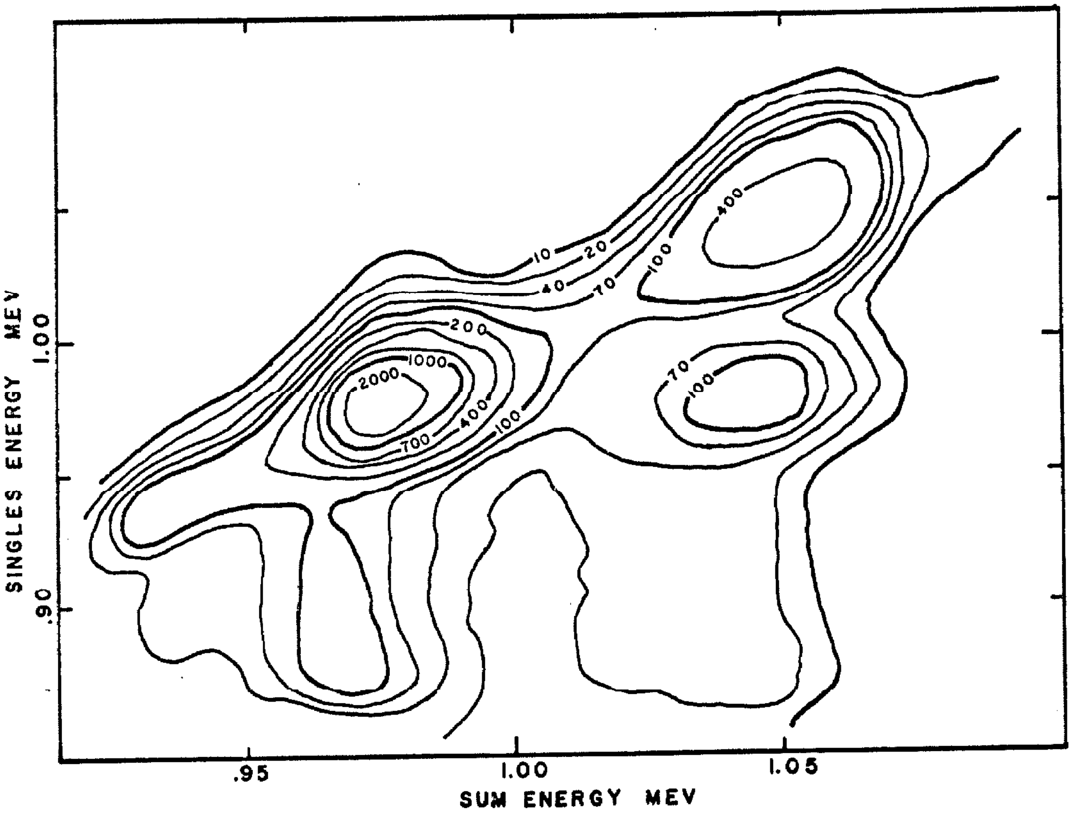

Figure 16

Contour plot of the region around the 1.06 MeV gamma K and L conversion electrons. The low energy shoulders are due to the effective backing thickness of 6 mg/cm$^2$ of mylar.

In Fig. 17 the parameters A and B as a function of detector spacing are shown. The effect of the separation contributes only to the term B/E, the linear term being unaffected. The size of the contribution is roughly linear in the detector separation since it is proportional to the solid angle subtended by the inactive region of the detection system. This effect has been studied by Reynolds and Persson32) for separations from .2 mm to .7 mm. They obtain similar results. At 500 keV they obtain a correction of about 4 percent to the beta spectrum of $P^{32}$ with a separation of .2 mm. In our experiments we are able to use separations ten times smaller than this, making these distortions negligible.

### d) Discussion

Because it is necessary to use source backings in these experiments the effects of source absorption and detector separation cannot be entirely eliminated. The effect of the source absorption is to add approximately 1 percent to the line width and to shift the line peak by less than 1 percent of the instrumental resolution. The detector separation introduces corrections to the shape factor through the term B/E. The value of B is smaller than 1/2 percent. In most cases we will be interested in shape factors of the form 1 + AW in which case this effect introduces a small correction to the linear term.

Taking these effects into account we have obtained for the shape factor of $P^{32}$

$$C(E) = k(1 - (.025 \pm .005)E + (.02 \pm .01)\frac{1}{E}).$$

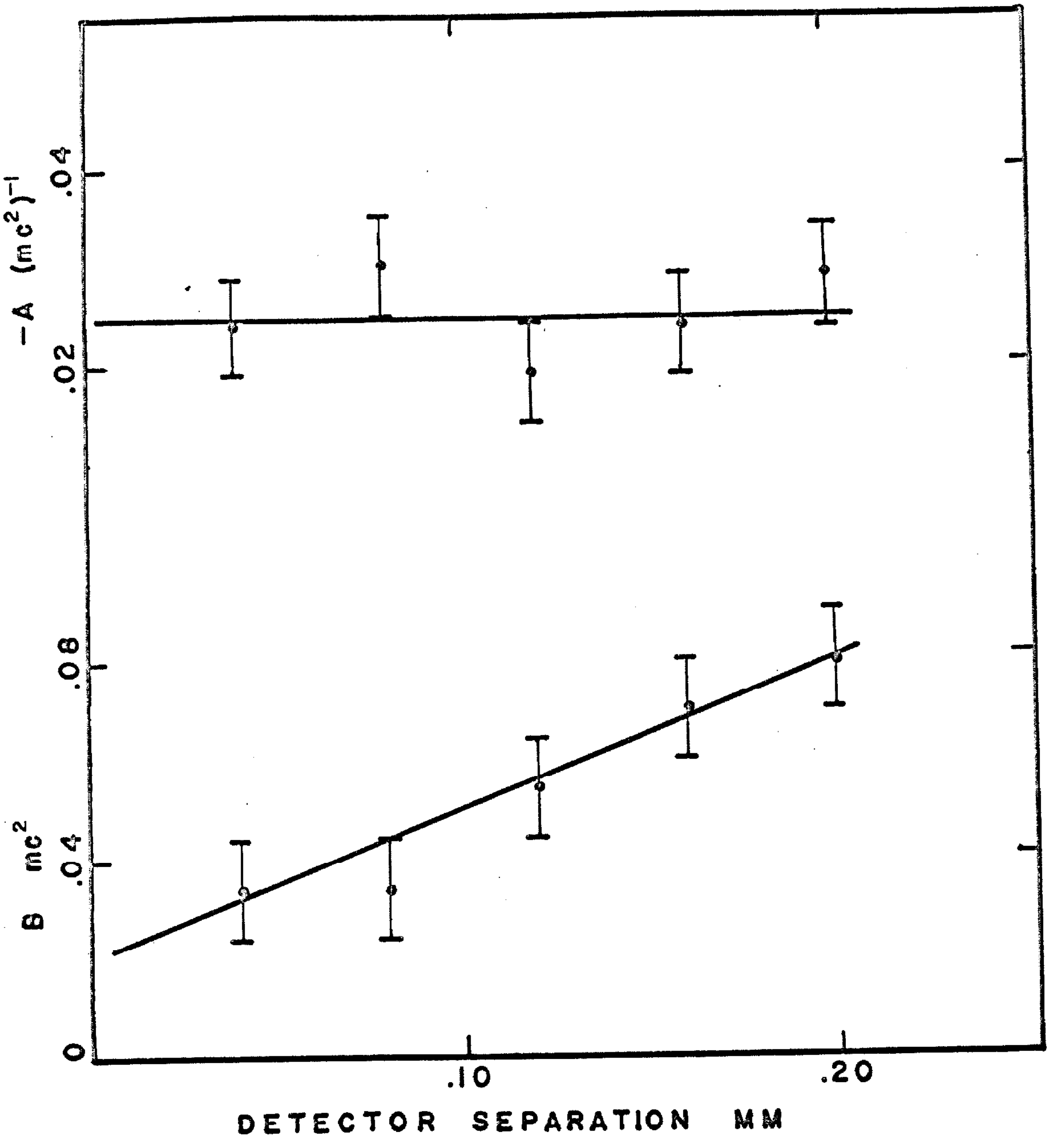

Figure 17

The coefficients A and B for the shape factor of $P^{32}$ as a function of detector separation.

TABLE 3

| Measurement | Form of Shape Factor | $A(mc^2)^{-1}$ | $B(mc^2)$ |
|---|---|---|---|
| Daniel | 1 + AW | -.04 ± .013 | |
| Novikov | 1 + AW + B/W | -.0249± .007 | .12 ± .05 |
| Langer | 1 + B/W | | .2 to .4 |
| Graham | 1 + B/W | | .16 |
| Chabre | 1 + AW | -.03 | |
| Lehmann | | 0 ± .01 | |
| Persson | | 0 ± .01 | |
| This Measurement | 1 + AW + B/W | -.025 ± 005 | .02 ± .01 |

The results of shape factor measurements on $P^{32}$. The measurement of Persson was done with solid state detectors, the remaining are magnetic spectrometer measurements.

This result is compared with those obtained using magnetic spectrometers. Table 3, taken from Lehmann[34)] summarizes a number of the more reliable measurements of the shape factor of $P^{32}$. We also include the result of Ref. 32 and this measurement, both of which were done using solid state detectors. The discrepancy in the last two measurements can be eliminated if the iterative procedure described in Appendix I is changed to correspond to that used in Ref. 32, where the shape factor C(E) was not included in the iteration procedure.

# VI. THE BETA DECAY OF $Tl^{207}$

The methods developed in the preceding chapters have been applied to the determination of the shape factor of the beta decay of $Tl^{207}$. The half-life of $Tl^{207}$ is 4.8 minutes and hence the spectrum shape factor is not amenable to measurements using a magnetic spectrometer. The decay proceeds primarily to the ground state of $Pb^{207}$, the branching ratio to the 900 keV state in $Pb^{207}$ being 0.16 percent 35). This leads effectively to a single beta-branch with no gamma rays to contribute to background.

$Tl^{207}$ is also an interesting nucleus from a theoretical point of view. The nucleus is immediately adjacent to the doubly magic $Pb^{208}$ which has a closed proton shell of $Z = 82$ and a closed neutron shell of $N = 126$. The level schemes of $Tl^{207}$ and $Pb^{207}$ are shown in Fig. 18. These levels are well understood in terms of the single particle model. This model predicts the proton hole in $Tl^{207}$ to be in $S_{1/2}$ orbital and the neutron hole in $Pb^{207}$ to be in a $P_{1/2}$ orbital. These predictions have been confirmed by the experiments of several workers 35,36,37).

In this work we have measured the energy spectrum of the beta branch to the ground state and the lifetime of $Tl^{207}$.

## i) Sources

The preparation of pure $Tl^{207}$ sources has not been possible until fairly recently. This is primarily due to the development of ion exchange techniques and solvent extraction techniques. In order

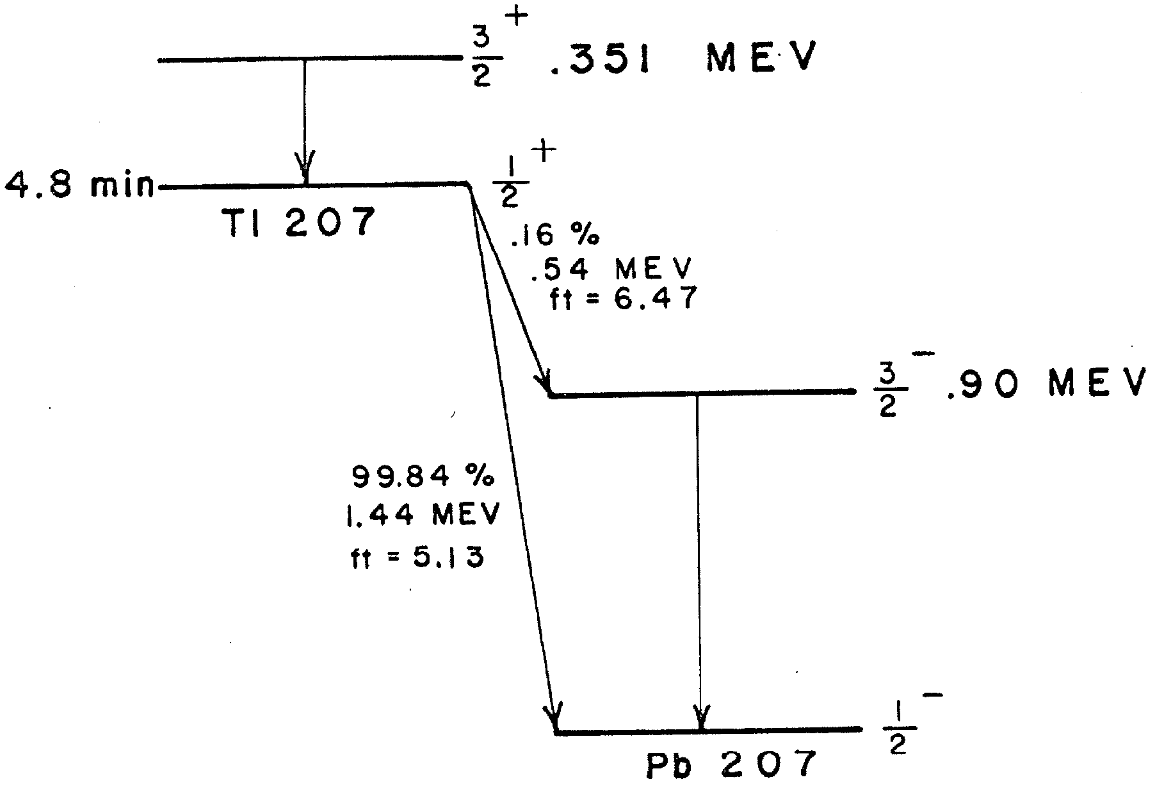

Figure 18

Level Schemes of $Pb^{207}$ and $Tl^{207}$

that the separation of $Tl^{207}$ is to be useful in the preparation of beta sources it is necessary that the time of preparation be short, of the order of one half life. We also require the resulting sources to be suitably thin to beta rays. Since the active area of the detectors used in these experiments is 1 $cm^2$, the sources must also be confined to an area small compared to 1 $cm^2$.

$Tl^{207}$ is not a member of a naturally occuring radioactive group, the longest living member of the 4n + 3 chain of which it is a daughter being 32.5 thousand year $Pa^{231}$. For this experiment we obtained a 1 mc source of $Ac^{227}$ by neutron irradiation of $Ra^{226}$ which was obtained commercially. It was then necessary to separate the $Ac^{227}$ from the $Ra^{226}$ and its daughters, since both families contain Pb, Bi and Tl isotopes which cannot be separated chemically. This was done by placing the $Ac^{227}$ and $Ra^{226}$ on an ion exchange column containing Dowex-50 38). $Ac^{227}$ can be eluted with 1NHCl, all other elements being strongly stuck on the column. The $Ac^{227}$ was then used as the primary source of activity for the remaining separations.

A number of intermediate separations were necessary to obtain sources of pure $Tl^{207}$. The $Ac^{227}$ was placed on a Dowex-50 ion-exchange column and allowed to come into equilibrium with its daughters (approximately 30 days). $Ac^{227}$ was then eluted with 1NHCl and 11.6 day $Ra^{223}$ was eluted with 12NHCl. The $Ra^{223}$ was then placed on a micro-column (free column volume of 15 μl) containing Dowex-50 and allowed to come to equilibrium with its daughters. Finally 36 minute $Pb^{211}$ was eluted with 2NHCl. The $Tl^{207}$ sources were prepared by solvent extraction from this solution.

The HCl solution of Pb, Bi, Po and Tl was brought to 6N. The Tl was oxidized to its $3^+$ state by adding bromine. The $Tl^{207}$ was then extracted into ethyl-ether[39)].

The beta sources were prepared on Formvar backings 15 μg/$cm^2$ thick. The Formvar foils were supported front and back by aluminum foil .01 mm thick. In order to confine the sources to a small area on the Formvar it was necessary to evaporate the ethyl-ether down to less than 1 μl before placing on the backing. The source area obtained in this way was about 1 $mm^2$. After evaporation of all the ether the sources were covered with a Formvar foil in order to prevent contamination of the detectors.

The efficiency with which the entire operation could be made was not high. The $Tl^{207}$ sources thus prepared had an initial activity of about 1 μc. This was not a problem, however, as the counting rate of about $10^4$ counts per second, acceptable by the electronics was the limiting factor on the allowable activity of the sources. Since the source preparation described results in carrier-free sources, the amount of material in the source contributes negligibly to the total thickness of source plus backing.

The separation of the Pb, Bi and Po isotope was essentially 100 percent. Figure 19 shows the gamma spectrum obtained with a sodium iodide counter from $Pb^{211}$ in equilibrium with all its daughters and that obtained after the $Tl^{207}$ solvent interaction. The gamma ray spectrum of the $Tl^{207}$ showed only the weak 900 keV

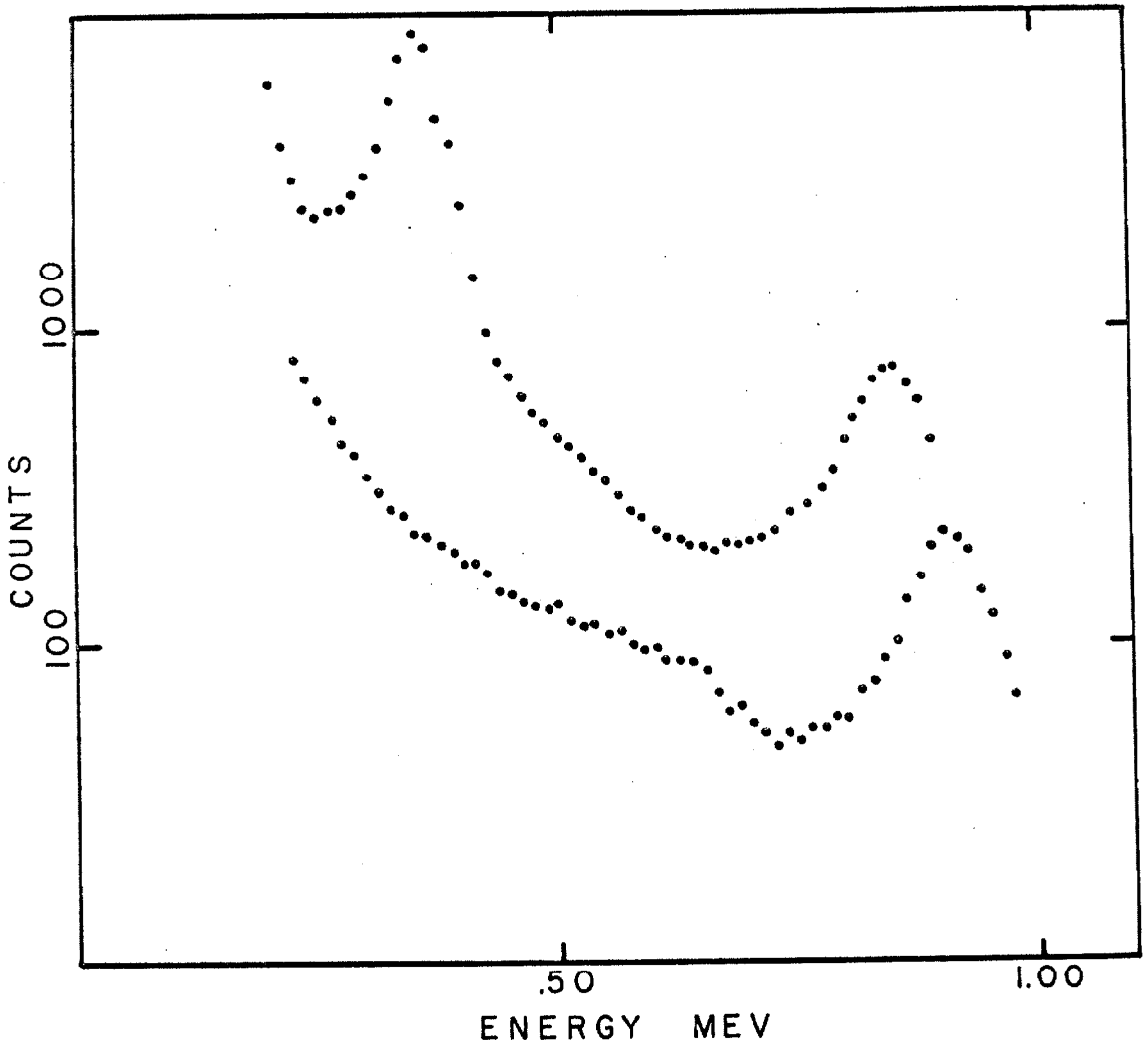

Figure 19

The upper curve shows the gamma spectrum of $Pb^{211}$ in equilibrium with its daughters. The 351 keV peak is due to the level in $Tl^{207}$, the 830 keV peak is due to a level in $Bi^{211}$. The lower curve shows the gamma spectrum after the thallium separation. The 900 keV peak is due to the level in $Pb^{207}$, the 351 keV peak has completely disappeared.

gamma ray.

## ii) Experiments

The experiments on $Tl^{207}$ were done with the same apparatus as described in Chapter V. For the determination of the energy spectrum the sum pulses were recorded in a multichannel analyzer. For the half-life measurements only a single detector was used.

### a) Half-Life Measurement

The half-life measurements were done by measuring the integral spectrum as a function of time. The output of the post amplifier was fed to a single channel integral discriminator. The output of the discriminator was counted in an RIDL multichannel analyzer operating in the time mode. The storage channel was incremented each 8 sec for 3200 sec. This represents about 11 half-lives. A typical time spectrum is shown in Fig. 20.

The results obtained for several runs were fitted in a least squares program to an exponential plus a background. It was sufficient to take the background as constant, no improvement in the fit was found by including a linear term. This indicates that there was no $Pb^{211}$ present in the $Tl^{207}$ sources.

### b) Energy Spectrum Measurements

The differential energy spectrum was measured by recording the summed pulse height spectrum from the two detectors. After preparing the $Tl^{207}$ sources, they were centered between the detectors and the cryostat was closed and flushed with dry helium. The

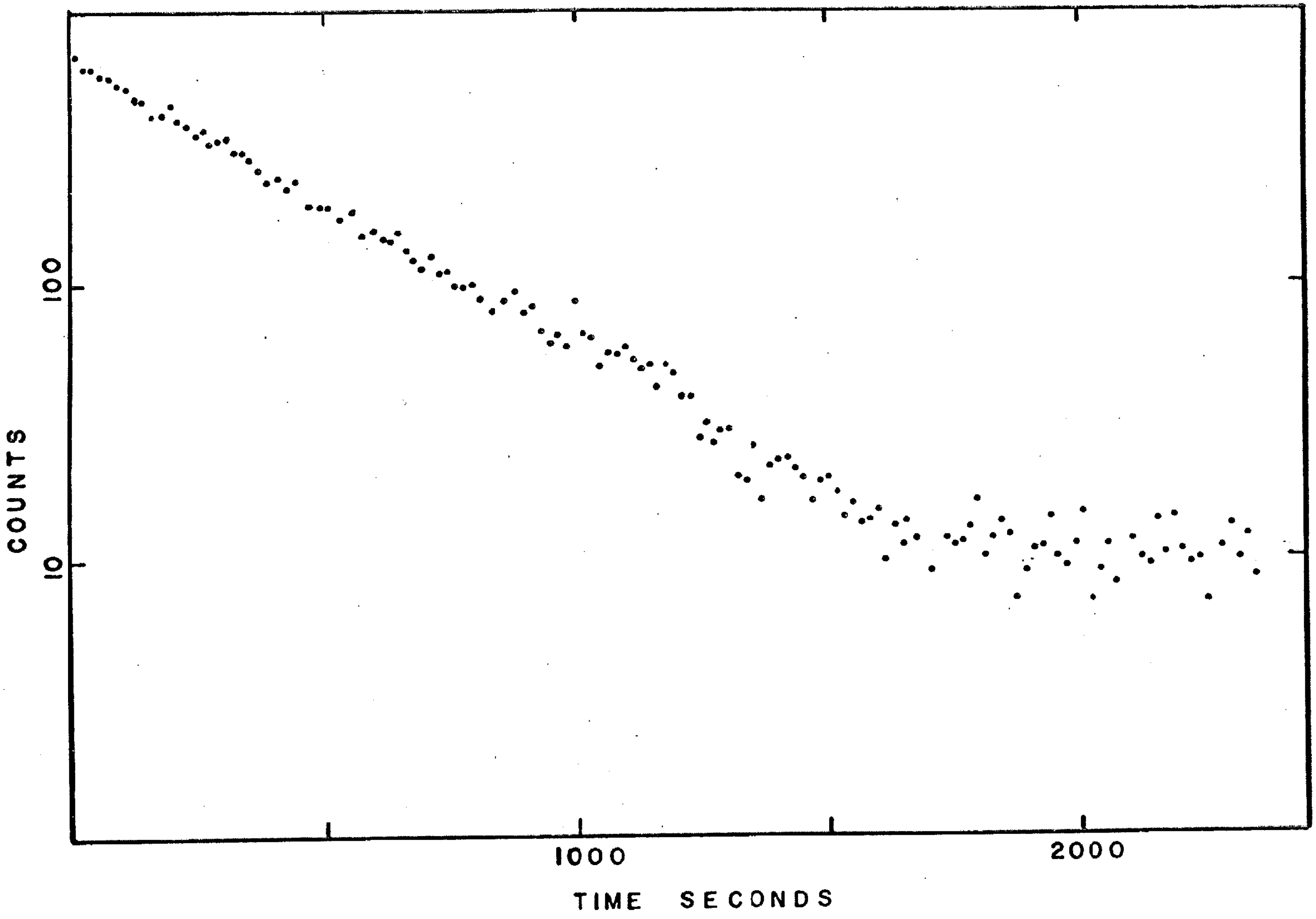

Figure 20

A typical time spectrum of the 4.8 min decay of $Tl^{207}$.

detectors were then cooled to liquid nitrogen temperatures before counting began. The total time taken for this procedure was generally 5 minutes. The pulse height spectrum was then recorded for two successive 10 minute periods. These spectra were compared to check for any long living activity due to incomplete separation and to make background corrections. After each run an energy calibration was done by recording the gamma spectrum of a $Co^{60}$ source placed near the cryostat. This also serves as a measurement of the instrumental line width and as a check on amplifier drifts.

The spectra obtained were analyzed by the procedure explained in Appendix I. The corrections due to the resolution were always less than 1 percent.

### iii) Results

The result of the half-life measurements was obtained by taking the weighted average of the individual runs. The result of 286 ± 2 sec agrees with previously reported results[40)].

Table 4 shows the results of the shape factor measurements. We give only the linear term. The fit was not improved by including the 1/W term, hence we conclude that the experiment was not sensitive enough to distinguish this from the linear term. The errors quoted for the individual runs are due only to statistics. To obtain an estimate of the other errors involved a least squares analysis was done on the individual runs. The values of $\chi^2$ obtained for the fit was 12.5. This indicates that there is probably some systematic contribution to the real errors. Finally, using the fact that

TABLE 4

| Run | Total Counts | $A(mc^2)^{-1}$ | Statistical Error |
|---|---|---|---|
| 1 | 197,000 | -.011 | .020 |
| 2 | 168,000 | .045 | .021 |
| 3 | 113,000 | .030 | .023 |
| 4 | 89,000 | .025 | .031 |
| 5 | 182,000 | .047 | .020 |
| 6 | 45,000 | .007 | .039 |
| 7 | 170,000 | .039 | .021 |
| 8 | 42,000 | -.009 | .040 |
| Total | 1,130,000 | .024 | .007 |
| Weighted Average = .024 ± .01 | | | |

Results of shape factor measurement of $Tl^{207}$. The coefficients are the least squares fit to $C(W) = K(1 + AW)$. The errors quoted are due to statistics only. The error in the weighted average is such that the $X^2$ of a fit to the individual runs is 1.

$$(ft)_{1/2} = 6150 \text{ sec} \tag{18}$$

when the sum of the squares of the matrix elements equals one, we obtain for the shape factor of $Tl^{207}$

$$C(W) = (.0423 \pm .0006)(1 + (.024 \pm .010)W). \tag{19}$$

iv) Discussion

We interpret the results of the measurement in terms of the single particle model which is expected to give good results for nuclei near closed shells. Blomqvist and Wahlborn[41)] have calculated single particle wavefunctions for the nuclei $Pb^{207}$, $Pb^{209}$, $Bi^{209}$, $Tl^{207}$. They used a Saxon-Wood type potential, including a spin-orbit interaction, and included pairing corrections. Separate sets of potential parameters were assigned to neutrons and protons, and were adjusted to fit existing energy level data.

Damgaard and Winther[42)] have used these wavefunctions to compute the single particle matrix elements pertinent to the first forbidden beta decay of $Tl^{207}$. The calculations include the effects of the radial dependence of the electron wavefunctions in the Coulomb field. Because of the isobaric spin dependence of the potential used to calculate the wavefunction, the matrix element $\langle \underline{\alpha} \rangle$ is calculated through the vector current continuity equation as indicated in Appendix III.

Using the values for the single particle matrix elements one calculates an $(ft)_{1/2}$ value about a factor of two too low. It is expected that the spherical core will be polarized by the motion of the single particle outside the core. If such is the case, the nucleons in the core can be expected to give significant contributions to the matrix elements. In Ref. (41) the size of this interaction between the core and the single particle is estimated by assuming a quadrupole interaction and calculating the amount of admixing of single particle states in the levels of $Tl^{207}$ and $Pb^{207}$. In the case of $Tl^{207}$ they find a 4 percent admixture (approximately .2 in amplitude) of a $d_{3/2}$ state in the $s_{1/2}$ ground state. In $Pb^{207}$ there is a 4 percent admixture of an $f_{5/2}$ state in the $P_{1/2}$ ground state. Vandenbusch et al.[35)] have measured the half-life of the 351 keV state in $Tl^{207}$ to be less than $0.6 \times 10^{-10}$ sec and the K conversion coefficient for the 351 keV gamma ray to be 0.239. Both of these values indicate that the level is depopulated by an M1 transition. The single particle transition is $d_{3/2} \rightarrow s_{1/2}$ for which the M1 transition is $\ell$ forbidden. The observed M1 rate thus arises entirely from the $d_{3/2}$ admixture.

For computational purposes we can treat the effects of configuration mixing by introducing effective charges, in a manner analogous to the electromagnetic transitions. In the case of beta decay two such charges are needed. They are obtained by writing

$$\begin{aligned} \langle \hat{\underline{r}} \rangle &= a \langle \hat{\underline{r}} \rangle \text{ s.p.} \\ \langle \underline{\sigma} \times \hat{\underline{r}} \rangle &= b \langle \underline{\sigma} \times \hat{\underline{r}} \rangle \text{ s.p.} \end{aligned} \qquad (20)$$

We assume the effect of the core polarization is to reduce the vector current. As stated above, the potential used in the computation of the wavefunctions is isobaric spin dependent, necessitating the addition of a term to the vector current in order that the continuity equation be fulfilled for the single particle current. The shape factor C(W) has been computed as a function of the parameters a and b. The result is

$$C(W) = \Big\{ 36.2 + (15.6a + 18.1b)^2 + .045W(-13.8 + (15.6a + 18.1b)(-2.8a + 37.2b)) \Big\} \times 10^{-4}.$$

The two experiments now determine two relations between a and b. These relations are shown in Fig. 21. The experimental result for the parameters is

$$\begin{aligned} a &= .83 \pm .10 \\ b &= .40 \pm .10. \end{aligned} \qquad (21)$$

In view of the significant amount of admixing of the $d_{3/2}$ state in the ground state of $Tl^{207}$, these results do not seem unreasonable. The beta transition $d_{3/2} \rightarrow P_{1/2}$ is of the same order of forbiddenness as the $s_{1/2} \rightarrow P_{1/2}$ decay. Hence one should expect rates of the same order of magnitude. The fact that the admixing decreases the rate is physically reasonable, since it is due to a reaction of the core to the motion of the single particle.

A proper treatment of the effect of the core nucleons would involve a totally antisymmetrized description of all the nucleons, since they are all capable of transforming. Attempts to treat the

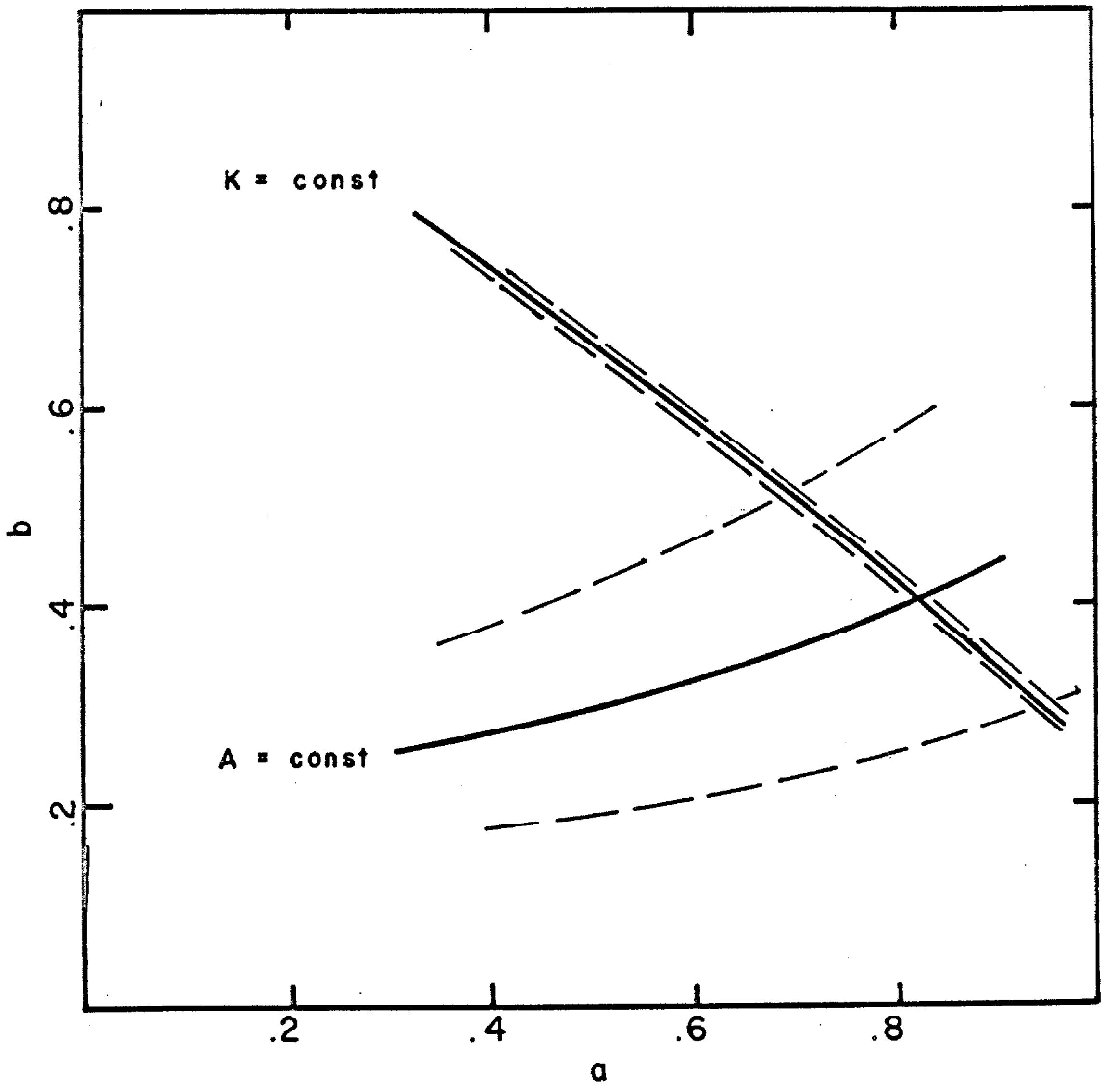

Figure 21

The "effective beta charges" a and b. The curves A = const. are curves of constant shape, the curves K = const. are curves of constant $(ft)_{1/2}$. The solid lines are the results of the shape factor and $(ft)_{1/2}$ measurements, the dashed lines are the experimental errors in these measurements.

effects of core nucleons by the construction of many particle states yield reasonable results for stationary quantities such as the energy, but meet with only limited success in the computation of transition rates.

## VII. CONCLUSIONS

We have presented a description of a $4\pi$ solid state beta spectrometer. In view of the fact that very little experimental information is available concerning the use of solid state detectors in the study of continuous beta spectra, we have presented the results of experiments to determine the properties of these detectors. We have seen that serious distortions in beta spectra result from electron scattering from the detector and the environment. These distortions cause the analysis of the experimental spectra to be extremely complicated. The results obtained are not accurate enough to measure shape factors of the order of 1 percent. In applications involving conversion electrons, such as $e^- - \gamma$ correlations, these detectors can be very useful because of their high solid angles and low charge collection times.

The essential feature of the $4\pi$ spectrometer is the complete dissipation of the beta particle energy in the sensitive volume of the detectors. We have seen that the effects of source absorption and detector separation in such spectrometers can lead to percent effects. The problem of source absorption was seen to be more serious than in the case of magnetic spectrometers because of possible multiple scattering. The effective source thickness was roughly three times the actual thickness. We have pointed out the problems arising from correlations between the assumed endpoint energy and the shape factor. In the case of solid state detectors it is necessary to treat both $W_0$ and the parameters in the shape factor as free parameters.

The measurement of the shape factor and $(ft)_{1/2}$ value of $Tl^{207}$ indicates substantial disagreement with shell model calculations. The fact that the core nucleons are expected to play a role in determining transition rates was suggested from electromagnetic data. The treatment of the core nucleons is extremely difficult and has been carried out in an approximate way. The consistency of such a treatment could be investigated by an investigation of the beta decay of several other short living isotopes near $Pb^{208}$.

Filmed as received

without page(s) 57.

Taking the inverse transform we obtain the final result

$$I(E) = O(E) - \frac{\sigma^2}{2} \frac{d^2}{dE^2} (O(E)) + \dots . \qquad (26)$$

The expansion is useful because of the small size of $\sigma$ obtained with solid state detectors. In all cases the corrections to the beta spectra were less than 1 percent.

## Solution of the Integral Equation for the Detection of Electrons by a Single Detector

The response function for the noise free detection of electrons by a single detector is

$$\begin{aligned} G(E,E') &= S(E)\ \delta(E - E') + \frac{(1 - S(E))}{E} \qquad & E \leq E' \\ &= 0 & E > E' \end{aligned} \qquad (27)$$

where $S(E)$ is the backscattering parameter and $E'$ is the incident electron energy. Putting this into the convolution integral for the output spectrum gives

$$O(E) = S(E)\ I(E) + \int_E^{E_0} \frac{(1 - S(E'))}{E'} I(E')\ dE' \qquad (28)$$

where $I(E)$ is the input beta spectrum, $O(E)$ is the observed spectrum and $E_0$ is the beta decay endpoint energy. The solution was obtained by iteration. In the first case $S(E)$ was treated as the unknown function. The function $I(E)$ was taken to be the known energy spectrum of the $P^{32}$ beta decay. Assuming a function $S_0(E)$ we calculate

$$O_1(E) = S_0(E)\ I(E) + \int_E^{E_0} \frac{(1 - S_0(E'))}{E'} I(E')dE'. \qquad (29)$$

For the second iteration $S_0(E)$ is corrected to be

$$S_1(E) = S_0(E) + \frac{(O_{obs}(E) - O_1(E))}{O_{obs}(E)} \tag{30}$$

where $O_{obs}(E)$ is the observed spectrum. The integral equation then gives a new $O_2(E)$ and so on. For not too unreasonable choices for $S_0(E)$ the procedure converges in four or five iterations. The solution is not sensitive to the initial $S_0(E)$.

In the second case I(E) is the unknown. The procedure is similar, the initial guess for I(E) being I(E) = O(E).

Determination of the Shape Factor

In all cases the data were corrected for the finite resolution. For the 4π counting geometry this corrected data was used in the determination of the shape factor. For the single detector, the result of the calculation above was used.

The spectra were fitted to the function

$$N(W)dW = \frac{1}{2\pi^3} F_0(Z,W)pW(W_0 - W)^2 L_0(r_0)C(W)dW. \tag{31}$$

In the case of $P^{32}$, C was taken as

$$C = K(1 + AE + B/E)$$

where E is the kinetic energy of the electron. For $Tl^{207}$

$$C = K(1 + AW).$$

A least squares fit was made to the data, treating $W_0$ and the parameters in C(W) as free parameters$^{43)}$. The following iterative procedure was used to minimize $\chi^2$.

1. Using the experimental energy calibration to determine $W_0$, a least-squares fit was done to the parameters in C(W).
2. Using the same energy calibration and the function C(W) determined in step (1), a Fermi-Kurie plot was computed. A new endpoint energy was obtained by fitting the Fermi-Kurie plot to a straight line and determining the zero crossing.
3. Using this new calibration, the procedure is repeated from step (1).

The procedure was continued until no significant change in the endpoint energy was obtained. It should be pointed out that the actual value for $W_0$ was taken from existing data. In the numerical analysis the energy of the electron is related to the channel in the pulse height spectrum by a calibration factor, and it is this calibration which is determined in the analysis.

# APPENDIX II

## ON THE CORRELATIONS BETWEEN $W_0$ AND THE SHAPE FACTOR

In this Appendix we will present results pertinent to the analysis of the spectra obtained with solid state detectors. In the case of solid state detectors it is not possible to analyse the data in the traditional manner. In high resolution studies with magnetic spectrometers very accurate energy calibration is possible. A determination of the endpoint of the beta spectrum is made by extrapolating the lower part of a Fermi-Kurie plot linearly until it crosses the energy axis. The important consideration is that the percentage error involved is determined primarily by the resolution of the instrument. This is typically one part in $10^3$ to $10^4$.

A similar situation does not exist for solid state counters. Generally one part in $10^3$ is an upper limit on the resolution. This is, in general, not a sufficiently accurate determination. In the following we will show that correlations in the shape factor and endpoint energy necessitate a more unified treatment of the parameters involved. Recent considerations of this problem[43)] seem to indicate this as a possible source of discrepancies in reported results of shape factor measurements.

For the purpose of this analysis, the energy spectrum of electrons may be written

$$N(W)\ dW = G(W)(W_0 - W)^2\ C(W) \qquad (32)$$

where G(W) is given by

$$G(W) = \frac{1}{2\pi^3} F_0(Z,W) pW \, L_0(r_0) \tag{33}$$

$F_0(Z,W)$ is the Fermi function, C(W) is the shape factor and $W_0$ is the endpoint energy. In the following we will consider G(W) as a known function of energy.

We consider the shape factor to be of the form

$$C(W) = K(1 + AW). \tag{34}$$

Calculations similar to the ones to be described have been performed including term B/W. No significant changes in the results were obtained with this form for the shape factor.

We have investigated with a computer the shape of the $\chi^2$ surface near the minimum resulting from a least squares fit to the parameters A and $W_0$. The $\chi^2$ surface was computed using varying fractions of the total spectrum. Figure 22 shows contour plots of $\chi^2$, using a value of 0.05 for A. The correlation is such that a .01 percent error in $W_0$ would cause a change in the best value of A of slightly more than 1/2 percent, that is a 10 percent error in A. In Table 5 we give the values of the parameters and the deviations at which the probability of obtaining a $\chi^2$ greater than that obtained with these parameters is 0.1. As expected the amount of the spectrum used in the fit decreases, the parameter A becomes very poorly determined. The precision with which $W_0$ can be determined is decreased because of the poorer statistics, however, the result is relatively insensitive to A. The signs associated with the

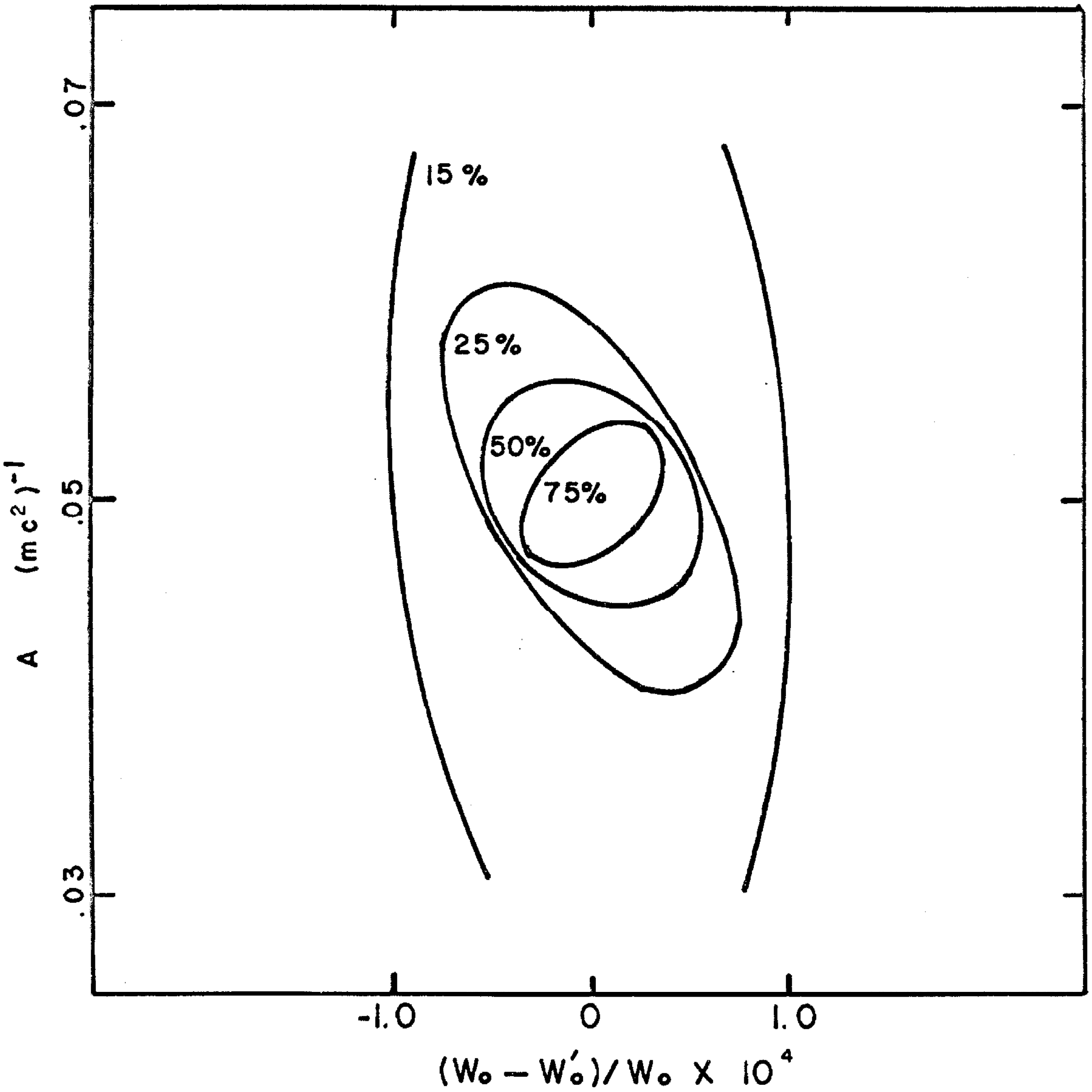

Figure 22

Contour plots of $X^2$ in the parameter space $W_0$, A using various fractions of the beta spectrum. The axis of the ellipse becomes aligned with the A axis when small percentages of the spectrum are used, and the curves become more elongated. This is due to the fact that A is determined essentially from the lower part of the spectrum.

TABLE 5

| % of Spectrum Used | Parameter Values for $X^2$ = min | | Change in Parameter Values at $P(X^2) = .1$ | |
|---|---|---|---|---|
| | $W_0$ | A | $\Delta W_0$ | $\Delta A$ |
| 75 | 3.000 | 0.050 | .0005 | .002 |
| 50 | 3.000 | 0.050 | .0005 | .006 |
| 25 | 3.000 | 0.050 | .0006 | .025 |
| 20 | 3.000 | 0.046 | .0009 | .035 |
| 15 | 3.000 | 0.037 | .0010 | .060 |
| 10 | 3.000 | 0.020 | .0015 | .10 |

Values of the parameters $W_0$ and A obtained from least squares fits to various percentages of the beta spectrum. The values in the last two columns give the amount by which the parameters must change to give a $X^2$ whose probability is 0.1.

deviations are meant to indicate that the correlation between $W_0$ and A always is such that an increase in $W_0$ produces a decrease in A. Hence, the errors involved are of a systematic nature.

In Fig. 23 we summarize a number of shape factor measurements of $P^{32}$. The shape factors have been linearized. The straight line is drawn with a slope corresponding to the correlation between $W_0$ and A obtained from the $X^2$ plots.

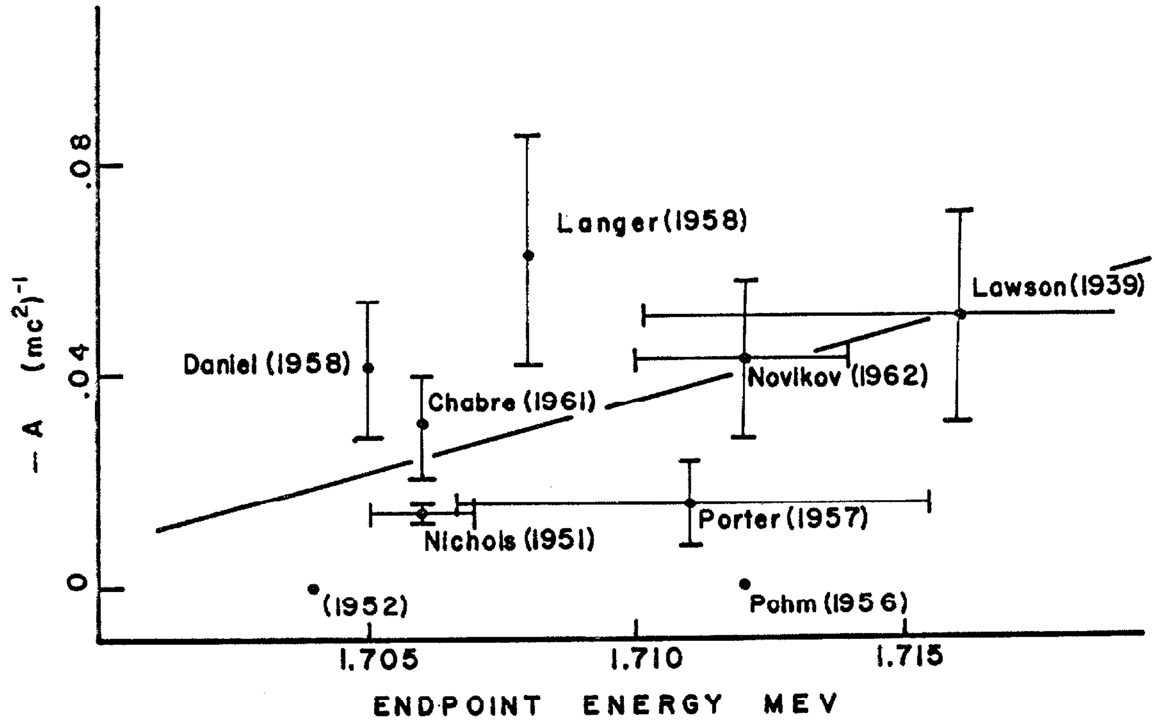

Figure 23

A plot of various measurements of the shape factor of the beta decay of $P^{32}$. The shape factors have been linearized by taking an average value of 1/W. The errors are those of the authors, where quoted. The straight line has a slope equal to the correlation obtained from the $X^2$.

# APPENDIX III

## SHAPE FACTOR FOR FIRST FORBIDDEN BETA DECAY

According to Ref.42 the beta spectrum shape can be written

$$N(W)dW = \frac{1}{2\pi^3} F_0(Z,W)pW(W_0-W)^2 L_0(r_0) C(W)dW \tag{35}$$

where $F_0(Z,W)$ is the Fermi function of Ref. 33, $r_0$ is the nuclear radius, and

$$L_0(r_0) = \frac{1}{2p^2F_0(Z,W)} \left(g_{-1}^2(r_0) + f_1^2(r_0)\right). \tag{36}$$

$C(W)$ can now be written to first order in $\xi = \frac{\alpha Z}{2r_0}$ as

$$C(W) = K_0^2 + K_1^2 + \frac{2W}{3\xi}(K_0J_o + K_1J_1) \tag{37}$$

where

$$K_0 = C_A\langle g'_{-1}\gamma_5\rangle - C_A\left(\frac{\alpha Z}{2}\right)\langle g'_1\, i\, \underline{\sigma}\cdot\underline{\hat{r}}\rangle$$

$$J_0 = -\, 2C_A\left(\frac{\alpha Z}{2}\right)^2\langle g'_1\, \gamma_5\rangle + \frac{6}{5}\, C_A\left(\frac{\alpha Z}{2}\right)^3\langle g'_{-1} i\underline{\sigma}\cdot\underline{\hat{r}}\rangle$$

$$K_1 = C_V\langle g'_{-1}\underline{\alpha}\rangle - C_V\left(\frac{\alpha Z}{2}\right)\langle g'_1 i\underline{\hat{r}}\rangle + 1C_A\left(\frac{\alpha Z}{2}\right)\langle g'_1\, \underline{\sigma}\times\underline{\hat{r}}\rangle$$

$$+ \frac{2\sqrt{2}}{3}C_V\left(\frac{\alpha Z}{2}\right)^2\frac{W_0}{3\xi}\langle g'_{-1}\, \underline{\alpha}\cdot\underline{T_1}^2\rangle$$

$$J_1 = -\,\frac{10}{3}C_V\left(\frac{\alpha Z}{2}\right)^2\langle g'_1\underline{\alpha}\rangle + \frac{6}{5}C_V\left(\frac{\alpha Z}{2}\right)^3\langle g'_{-1} i\underline{\hat{r}}\rangle + 2C_A\left(\frac{\alpha Z}{2}\right)\langle g'_{-1}\underline{\sigma}\times\underline{\hat{r}}\rangle$$

$$-\,\frac{2\sqrt{2}}{3}C_V\left(\frac{\alpha Z}{2}\right)^2\langle g'_1\, \underline{\alpha}\cdot\underline{T_1}^2\rangle$$

and

$$g'_{\kappa}(r) = \frac{g_{\kappa}(r)}{g_{\kappa}(r_0)} = \alpha_0^{\kappa} + \alpha_2^{\kappa}\left(\frac{r}{r_0}\right)^2 + \alpha_4^{\kappa}\left(\frac{r}{r_0}\right)^4 .$$

The notation $\langle g'_{\kappa}\, 0_{\beta}\rangle$ for the nuclear matrix elements indicates that the radial dependence of the Coulomb wavefunctions is to be included. These matrix elements are tabulated in Table 6 . The matrix elements $\langle \underline{\alpha}\rangle$ are related to $\langle i\hat{\underline{r}}\rangle$ and $\langle \underline{\alpha}\cdot \underline{T}_1{}^2\rangle$ through the continuity equation. In the presence of the Coulomb field this is written, assuming $V = \frac{Ze}{r_0}\left(\frac{3}{2} - \frac{1}{2}\left(\frac{r}{r_0}\right)^2\right)$

$$-\underline{\nabla}\cdot \underline{J}_V = \frac{3}{2}\left(\frac{\alpha Z}{r_0}\right)\left(1 - \frac{1}{3}\left(\frac{r}{r_0}\right)^2\right)\rho_V + \frac{\partial \rho_V}{\partial t} \tag{38}$$

where $\underline{J}_V$ is the space component of the nuclear beta current and $\rho_V$ is the time component. Forming matrix elements we obtain

$$\left\langle \underline{\alpha}\left(\frac{r}{r_0}\right)^{2n}\right\rangle = 3\left(\frac{\alpha Z}{2}\right)\left\langle i\,\hat{\underline{r}}\left(\frac{r}{r_0}\right)^{2n}\left[1 - \frac{1}{3}\left(\frac{r}{r_0}\right)^2 + \frac{W_0}{3\xi}\right]\right\rangle - \delta_{n0}\,\frac{1}{\sqrt{2}} \left\langle \underline{\alpha}\cdot\underline{T}_1{}^2\left(\frac{r}{r_0}\right)^{2(n-1)}\right\rangle \tag{39}$$

with $\delta_{n0} = 0 \quad n = 0$

$\qquad = 1 \quad n \neq 0.$

TABLE 6

| Matrix Element | $K_0$ | $J_0$ | $K_1$ | $J_1$ |
|---|---|---|---|---|
| $C_A\langle\gamma_5\rangle$ | -.247 | -.240 | | |
| $C_A\left(\frac{\alpha Z}{2}\right)\langle i\underline{\sigma}\cdot\underline{\hat{r}}\rangle$ | -.186 | -.191 | | |
| $C_V\langle\underline{\alpha}\rangle$ | | | .255 | .254 |
| $C_V\left(\frac{\alpha Z}{2}\right)\langle i\underline{\hat{r}}\rangle$ | | | .099 | .102 |
| $C_A\left(\frac{\alpha Z}{2}\right)\langle\underline{\sigma}\times\underline{\hat{r}}\rangle$ | | | .181 | .186 |
| $C_V\left(\frac{\alpha Z}{2}\right)^2\langle\underline{\alpha}\cdot\underline{T_1{}^2}\rangle$ | | | .023 | .022 |

Matrix elements for the first forbidden ground state decay of $Tl^{207}$

# APPENDIX IV

## RESOLUTION AND ELECTRONIC NOISE

In the following we will assume that the frequency response of the amplifying system is determined by a single integrating and differentiating time constant. The gain of the system is then

$$G(\omega) = G_0 \frac{\omega^2 \tau^2}{(1 + \omega^2 \tau^2)^2} \tag{40}$$

where $\omega$ is the frequency and $\tau$ is the integrating and differentiating time constant. The mean square noise voltage is then given by

$$\overline{V^2} = \int_0^\infty v^2(\omega)\ G(\omega)\ d\omega\ . \tag{41}$$

All voltages will be referred to the amplifier input, and expressed in terms of the equivalent energy of an incident particle which would produce a pulse of this size by multiplying by $\omega \frac{C_{in}}{e}$, $C_{in}$ being the input capacity and e the electronic charge.

Shot Noise

The shot noise due to grid leak currents and detector currents is

$$\sigma_{sh}^2 = w^2 \frac{I_d \ \tau}{2e} \tag{42}$$

where $I_d$ is the sum of the grid current and the detector current, and w is the average energy required to produce an electron-hole pair.

The Johnson noise due to the input resistance $R_g$ is

$$\sigma_R^{\,2} = \left(\frac{w}{e}\right)^2 \frac{kT}{R_g} \cdot \frac{\tau}{2} \quad . \tag{43}$$

1/f Noise

There is a component of the noise in tubes and transistors equal to $A_f/f$. This contributes $\frac{wC_{in}}{e} \sqrt{\frac{A_f}{2}}$ to the input noise.

Plate or Collector Shot Noise

The plate current drawn by tubes, or collector current drawn by transistors, contributes to the noise

$$\sigma^2 = \left(\frac{wC_{in}}{e}\right)^2 \frac{2.5}{g_m} \frac{kT_e}{2\tau} \tag{44}$$

where $g_m$ is the transconductance of the device, and $T_e$ is the electron temperature.

The total input noise is now

$$\sigma_{tot}^2 = \left(\frac{w}{e}\right)^2 \left[\left(\frac{eI_d}{2} + \frac{kT}{2R_g}\right) \tau + \frac{2.5}{g_m} \cdot \frac{kT_e}{2} \cdot \frac{C_{in}^{\,2}}{\tau} + \frac{A_f}{2} C_{in}^{\,2}\right] \tag{45}$$

During these investigations the performance of several types of amplifiers, including tubes and field effect transistors as the input stage, has been checked. The best resolution obtained for electrons was 3 keV with a field effect transistor input. Although cooling of these transistors should reduce the noise level somewhat, we had little success in efforts to improve the resolution with cooling.

## REFERENCES

1. E.Z. Fermi, Phys. 88, 161 (1934).
2. T.D. Lee and C.N. Yang, Phys. Rev. 104, 254 (1956).
3. H. Frauenfelder, R. Bobone, E. von Goder, N. Levine, H.R. Lewis, R.N. Peacock, A. Rossi and G. De Pasquali, Phys. Rev. 106, 386 (1957).
4. J.M. Robson, Phys. Rev. 100, 933 (1955).
5. W.B. Hermannsfeldt, R.L. Burman, P. Stähelin, J.S. Allen, and T.H. Braid, Bull. Am. Phys. Soc. 4, 77 (1959).
6. M.A. Clark, J.M. Robson, and R. Nathans, Phys. Rev. Letters, 1, 100 (1958).
7. P.J. van Heerden, Dissertation, "The Crystal Counter", Utrecht, (1946).
8. K.G. McKay, Phys. Rev. 76, 1537 (1949).
9. F.S. Walter, J.W.T. Dabbs and L.D. Roberts, Bull. Am. Phys. Soc. 3, 181 (1958).
10. R.L. Williams and P.P. Webb, IRE Trans. of Nucl. Sci. NS 9, 160 (1962).
11. G. Ainsel, P. Baruch and O. Smulkowski, IRE Trans. of Nucl. Sci. NS 8, 21 (1961).
12. J.L. Blankenship, IRE Trans. of Nucl. Sci. NS 7, 192 (1960).
13. E.M. Pell, J. Appl. Phys. 31, 291 (1960).
14. H.A. Bethe, Z. Physik, 76, 293 (1938).
15. H.A. Bethe, Handbuch der Physik, Vol 24, 273, Julius Springer (Berlin 1933).
16. C. Møller, Ann. Physik 14, 531 (1932).
17. W. Heitler, The Quantum Theory of Radiation, Oxford University Press (London 1944).

18. O. Klein and K. Nishina, Z. Physik 52, 853 (1929).

19. H.A. Bethe, Ann. Physik 5, 325 (1940).

20. G.D. Archard, J. Appl. Phys. 32, 1505 (1961).

21. U. Fano, Phys. Rev. 72, 26 (1947).

22. J.L. Blankenship, IRE Trans. of Nucl. Sci. NS 11, 373 (1964).

23. W. Bothe, Z. Naturforsch. 4a, 542 (1949).

24. E.J. Sternglass, Phys. Rev. 95, 345 (1954).

25. J.M. MacKenzie, and C.T. Ewan, IRE Trans. of Nucl. Sci. NS 8, 50 (1961).

26. O.D. Barnes and L. Smith, J. Phys. Chem. 61, 326 (1957).

27. P.F. Peppard, G.W. Mason and S.W. Moline, J. Inorg. and Nucl. Chem. 5, 141 (1957).

28. J. Lehmann, Nuclear Phys. 68, 141 (1965).

29. H. Daniel, Nuclear Phys. 31, 293 (1962).

30. H. Hamilton, L.M. Langer, R.L. Robinson and W.G. Smith, Phys. Rev. 112, 945 (1958).

31. D.A. Howe, L.M. Langer, Phys. Rev. 124, 519 (1961).

32. J. Reynolds and B. Persson, Nucl. Instr. & Meths. 33, 77 (1965).

33. C.P. Bhalla and M.E. Rose, ORNL 3207 (1962).

34. J. Lehmann, Nuclear Phys. 68, 141 (1965).

35. S.E. Vandenbosch, C.V.K. Baba, P.R. Christensen, O.B. Nielsen and H. Nordby, Nuclear Phys. 41, 482 (1963).

36. W.G. Proctor, Phys. Rev. 79, 35 (1950).

37. B.L. Cohen, R.E. Price and S. Mayo, Nuclear Phys. 20, 370 (1960).

38. R.M. Diamond, K. Street, Jr., and G.T. Seaborg, J. Am. Chem. Soc. 76, 1461 (1954).

39. G.H. Morrison and H. Freiser, Solvent Extraction in Analytical Chemistry (John Wiley and Sons, New York, 1957).

40. B.W. Sargent, L. Yaffe, and A.P. Gray, Can. J. Phys. 31, 235 (1953).

41. J. Blomqvist and S. Wahlborn, Ark. Fys. 16, 545 (1960).

42. J. Damgaard and A. Winther, Nuclear Phys. 54, 615 (1964).

43. H. Beekhuis and H. de Waard, Nuclear Phys. 74, 459 (1965).

6a) R.J. Finkelstein and S.A. Moskowski, Phys. Rev. 95, 1695 (1954).

6b) M. Ross, Phys. Rev. 104, 1736 (1956).